

## RESEARCH ARTICLE

10.1002/2016JD024818

## Key Points:

- Precipitation  $\delta^{18}\text{O}$  over the Tibetan Plateau is simulated with a global climate model
- Predicted precipitation  $\delta^{18}\text{O}$  over Tibet agrees with sparsely available observations
- Extreme events analysis explains spatial and temporal variations in  $\delta^{18}\text{O}$

## Correspondence to:

T. A. Ehlers,  
todd.ehlers@uni-tuebingen.de

## Citation:

Li, J., T. A. Ehlers, S. G. Mutz, C. Steger, H. Paeth, M. Werner, C. J. Poulsen, and R. Feng (2016), Modern precipitation  $\delta^{18}\text{O}$  and trajectory analysis over the Himalaya-Tibet Orogen from ECHAM5-wiso simulations, *J. Geophys. Res. Atmos.*, 121, 10,432–10,452, doi:10.1002/2016JD024818.

Received 20 JAN 2016

Accepted 11 AUG 2016

Accepted article online 15 AUG 2016

Published online 20 SEP 2016

## Modern precipitation $\delta^{18}\text{O}$ and trajectory analysis over the Himalaya-Tibet Orogen from ECHAM5-wiso simulations

Jingmin Li<sup>1,2</sup>, Todd A. Ehlers<sup>1</sup>, Sebastian G. Mutz<sup>1</sup>, Christian Steger<sup>2</sup>, Heiko Paeth<sup>2</sup>, Martin Werner<sup>3</sup>, Christopher J. Poulsen<sup>4</sup>, and Ran Feng<sup>4,5</sup>

<sup>1</sup>Department of Geosciences, University of Tuebingen, Tuebingen, Germany, <sup>2</sup>Institute of Geography and Geology, University of Wuerzburg, Wuerzburg, Germany, <sup>3</sup>Climate Science Division, Alfred Wegener Institute, Bremerhaven, Germany, <sup>4</sup>Department of Earth and Environmental Sciences, University of Michigan, Ann Arbor, Michigan, USA, <sup>5</sup>National Center for Atmospheric Research, Boulder, Colorado, USA

**Abstract** Variations in oxygen isotope ratios ( $\delta^{18}\text{O}$ ) measured from modern precipitation and geologic archives provide a promising tool for understanding modern and past climate dynamics and tracking elevation changes over geologic time. In areas of extreme topography, such as the Tibetan Plateau, the interpretation of  $\delta^{18}\text{O}$  has proven challenging. This study investigates the climate controls on temporal (daily and 6 h intervals) and spatial variations in present-day precipitation  $\delta^{18}\text{O}$  ( $\delta^{18}\text{O}_p$ ) across the Tibetan Plateau using a 30 year record produced from the European Centre/Hamburg ECHAM5-wiso global atmospheric general circulation model (GCM). Results indicate spatial and temporal agreement between model-predicted  $\delta^{18}\text{O}_p$  and observations. Large daily  $\delta^{18}\text{O}_p$  variations of  $-25$  to  $+5\%$  occur over the Tibetan Plateau throughout the 30 simulation years, along with interannual  $\delta^{18}\text{O}_p$  variations of  $\sim 2\%$ . Analysis of extreme daily  $\delta^{18}\text{O}_p$  indicates that extreme low values coincide with extreme highs in precipitation amount. During the summer, monsoon vapor transport from the north and southwest of the plateau generally corresponds with high  $\delta^{18}\text{O}_p$ , whereas vapor transport from the Indian Ocean corresponds with average to low  $\delta^{18}\text{O}_p$ . Thus, vapor source variations are one important cause of the spatial-temporal differences in  $\delta^{18}\text{O}_p$ . Comparison of GCM and Rayleigh Distillation Model (RDM)-predicted  $\delta^{18}\text{O}_p$  indicates a modest agreement for the Himalaya region (averaged over  $86^\circ$ – $94^\circ\text{E}$ ), confirming application of the simpler RDM approach for estimating  $\delta^{18}\text{O}_p$  lapse rates across Himalaya.

### 1. Introduction

Long-term, multiparameter climate proxy records from the Tibetan Plateau (Figure 1a) and its surrounding areas have enabled reconstructions of climate change and paleoelevation over geologic (million year) time scales. A large number of stable isotope analyses, particularly  $\delta^{18}\text{O}$  from soil carbonate nodules ( $\delta^{18}\text{O}_{\text{carbonate}}$ ), have been conducted in recent years over the Tibetan Plateau [e.g., *Graham et al.*, 2005; *Rowley and Currie*, 2006; *DeCelles et al.*, 2007; *Garzzone*, 2008]. These  $\delta^{18}\text{O}_{\text{carbonate}}$  observations record the  $\delta^{18}\text{O}$  composition of precipitation ( $\delta^{18}\text{O}_p$ ). However, interpretations of past climate and the elevation history of the Tibetan Plateau from  $\delta^{18}\text{O}$  records rely upon our understanding of present-day climate- $\delta^{18}\text{O}$  relationships. This study is motivated by deficiencies in our current knowledge of the climate and topographic controls on  $\delta^{18}\text{O}$  across the Himalaya-Tibet region. We provide an analysis of the modern predicted and observed  $\delta^{18}\text{O}_p$  to facilitate future studies that interpret paleorecords of  $\delta^{18}\text{O}$ .

A growing number of recent studies report observed Tibetan  $\delta^{18}\text{O}_p$  and the  $\delta^{18}\text{O}$  composition of surface waters. Observational records in remote regions like the Tibetan Plateau are sparse in both their spatial coverage and temporal coverage. The sparseness of these records inhibits a detailed understanding of the underlying mechanisms for observed variations in  $\delta^{18}\text{O}_p$ . For example, the Global Network for Isotopes in Precipitation includes only one station near Lhasa on the Tibetan Plateau. The Institute of Tibetan Plateau Research in China has established a continuous observation network of  $\delta^{18}\text{O}_p$  on the Tibetan Plateau to augment the Lhasa station [e.g., *Tian et al.*, 1997; *Yao et al.*, 1999; *Tian et al.*, 2007; *Liu et al.*, 2010]. Observed  $\delta^{18}\text{O}_p$  from this network suggests a strong temperature effect on  $\delta^{18}\text{O}_p$  in the northeastern Tibetan Plateau and strong precipitation amount effects in the central and southern Tibetan Plateau [e.g., *Tian et al.*, 1997; *Yao et al.*, 1999; *Tian et al.*, 2007; *Liu et al.*, 2010]. In addition, *Hren et al.*, 2009 reported  $\delta^{18}\text{O}$  data from 191 streams

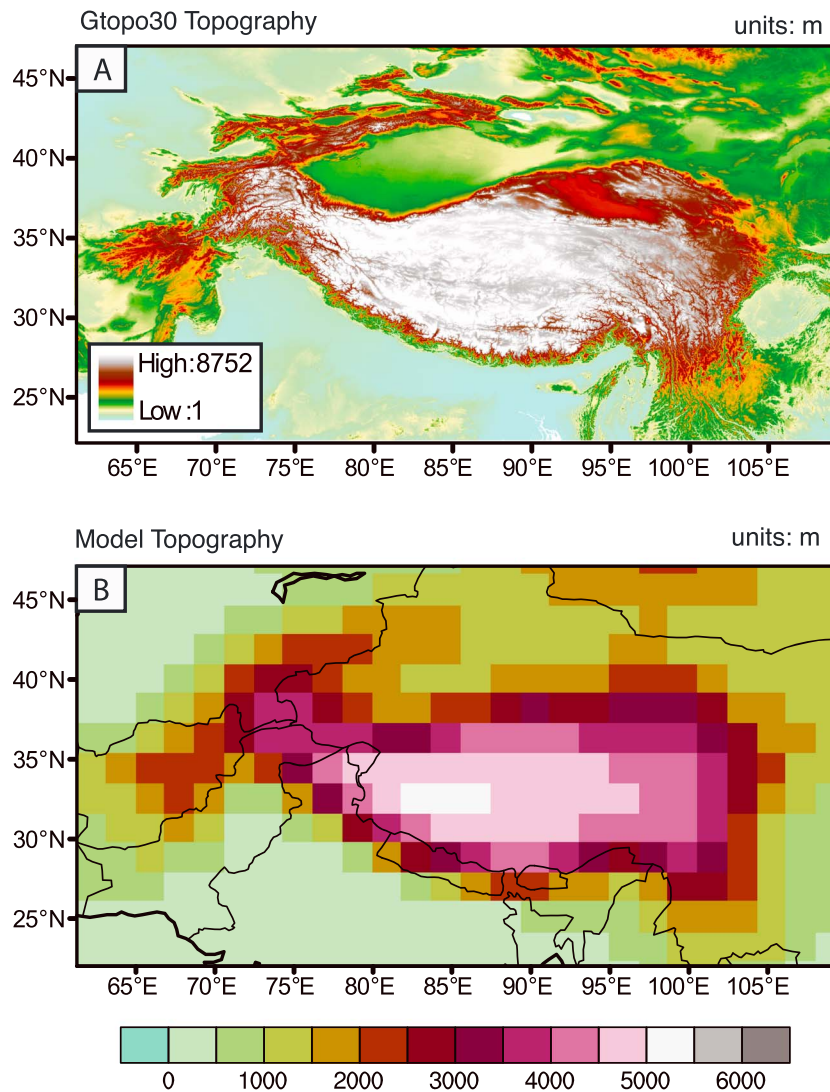


**Figure 1.** Topography of the Tibetan Plateau region from (a) GTOPO30 topography and (b) ECHAM5 model topography at resolution T63. The individual mountain ranges are not clearly represented by the model topography.

across the Himalaya and Tibetan Plateau and suggest that a mixing of moisture sources produced misfits of 1–3 km between observed and predicted catchment hypsometric elevations for the water source areas in the central Tibetan Plateau. Yao *et al.* [2013] summarize  $\delta^{18}\text{O}$  observations from existing precipitation and ice core data in the Tibetan Plateau region and identify three distinct domains of  $\delta^{18}\text{O}$ . These domains include a northern Tibetan Plateau and southern Tibetan Plateau region, with a transition zone in between them. These previous studies document complex spatial and temporal variations in  $\delta^{18}\text{O}$  across the Tibetan Plateau region. However, the limited spatial and temporal resolution of these records, as well as the short record length, inhibits a detailed analysis of the key atmospheric processes influencing  $\delta^{18}\text{O}_p$  across the Tibet Plateau.

Isotope tracking general circulation models with explicit calculation of stable water isotopes have made advances in predicting  $\delta^{18}\text{O}_p$  as a function of modern, paleoclimatological, and geologic processes [e.g., Armengaud *et al.*, 1998; Hoffmann *et al.*, 1998; Werner *et al.*, 1998, 2011; Cole *et al.*, 1999; Jouzel *et al.*, 2000]. Such isotope tracking model-based approaches have several advantages over observational approaches for understanding what processes influence water isotopes. These advantages include (1) simulation of long and continuous records of  $\delta^{18}\text{O}_p$  over a range of timescales (hourly, daily, monthly, yearly, and decadal) [e.g., Hoffmann *et al.*, 1998]; (2) availability of corresponding simulated climatological data for identification of the

controlling factors of  $\delta^{18}\text{O}_p$ ; these data include either diagnostic or derived values such as temperature, precipitation amount, vapor source, and transport distance [e.g., *Insel et al.*, 2013; *Jeffery et al.*, 2012]; and (3) broad spatial coverage in predicted  $\delta^{18}\text{O}_p$  that can be related to land cover and topography [e.g., *Feng et al.*, 2013; *Insel et al.*, 2012; *Poulsen et al.*, 2010]. Thus, while observational approaches are essential for documenting spatial and temporal patterns in  $\delta^{18}\text{O}_p$ , isotope tracking models provide an important tool for understanding the physical processes associated with observations.

Water isotopes modeling studies of modern and paleorainfall have been successfully conducted over a range of settings including South America, western U.S., Tibet, and Antarctica. Modeling studies of the Andes and western North America Cordillera [*Ehlers and Poulsen*, 2009; *Poulsen et al.*, 2010; *Insel et al.*, 2012; *Jeffery et al.*, 2012; *Feng et al.*, 2013] find that uplift-induced changes in atmospheric circulation, precipitation, and local mixing conditions could all contribute to changing distributions of  $\delta^{18}\text{O}_p$  across topography and can lead to biases in paleoelevation estimates of hundreds to thousands of meters. *Vuille and Werner* 2005 investigate the influence of the South American Summer Monsoon (SASM) on  $\delta^{18}\text{O}_p$  and demonstrated a significant negative association between  $\delta^{18}\text{O}_p$  and SASM over the Amazon basin, SE South America, and the central Andes. *Sturm et al.* [2007] document the influence of the South Atlantic Convergence Zone on the isotopic composition of precipitation and demonstrate that  $\delta^{18}\text{O}_p$  integrates variations in both precipitation and circulation.

However, water isotope tracking and climate modeling studies of the Tibetan Plateau are limited. Several studies have addressed the effect of the Tibetan Plateau on regional climate. For example, climate modeling studies have documented that surface uplift of the Tibetan Plateau leads to changes in moisture sources and precipitation by affecting the Indian Summer Monsoon, jet stream, and atmospheric thermostructure [e.g., *Ruddiman and Kutzbach*, 1989; *Boos and Kuang*, 2010; *Ma et al.*, 2014]. Previous water isotope modeling studies of the Tibetan Plateau [e.g., *Vuille et al.*, 2005] investigated the influence of the Asian monsoon on  $\delta^{18}\text{O}_p$  using the European Centre/Hamburg ECHAM4-wiso atmospheric model and found that variations in the amount of precipitation provide a first-order negative relationship with  $\delta^{18}\text{O}_p$  and also that  $\delta^{18}\text{O}_p$  variations in this region are sensitive to fluctuations in the Asian monsoon intensity. *Gao et al.* [2015] applied empirical orthogonal functions from the  $\delta^{18}\text{O}_p$  outputs of the LMDZiso model and reconstructed annual  $\delta^{18}\text{O}_p$  data with a  $2.5 \times 3.75^\circ$  resolution over the Tibetan Plateau. *He et al.* [2015] used a combination of in situ measurements with satellite data and atmospheric general circulation modeling. They revealed that the atmospheric convective activity over the Indian continent correlated with the summer precipitation isotopologue composition over southern Tibet. Based on the previous work, the various factors which can influence  $\delta^{18}\text{O}_p$  can be summarized as (1) temperature (temperature effect) and changes of the atmospheric thermostructure, (2) precipitation (amount effect) and changes of the precipitation scheme, and (3) changes in vapor sources and atmospheric circulation.

In this study, we complement previous work by using an isotope tracking global atmospheric general circulation model (GCM) to estimate modern  $\delta^{18}\text{O}_p$  variations across the Tibetan Plateau. Our emphasis is on regional-scale variations in  $\delta^{18}\text{O}_p$  that emerge from analysis of the 30 year predicted climatology. The model is forced with the present-day boundary conditions including sea surface temperatures, greenhouse gas concentrations, and orbital boundary conditions. Model results are used to identify the physical processes responsible for these variations based on a 30 year model simulation. The questions addressed in this manuscript include (1) how well does ECHAM5-wiso agree with newly available observations, (2) what processes control the minimum/maximum daily  $\delta^{18}\text{O}_p$  values over the Tibetan Plateau, and (3) how well does a simplified 1-D Rayleigh Distillation Model (RDM) of predicted  $\delta^{18}\text{O}_p$  across the Himalaya topography compare to GCM-derived estimates? This study presents an analysis of predicted  $\delta^{18}\text{O}_p$  variations that compliment spatially and temporally limited observations of  $\delta^{18}\text{O}_p$ . Our documentation of these variations has potential benefit for geoscience studies investigating paleo, proxy records of  $\delta^{18}\text{O}_p$  preserved in the sedimentary record that are limited in their understanding  $\delta^{18}\text{O}_p$  variability across the plateau.

## 2. Methods

### 2.1. The ECHAM5-Wiso Isotope-Enabled GCM

ECHAM5 is the fifth version of an atmospheric general circulation model designed to simulate climate. A full description of the ECHAM5 model and its formulation can be found in *Roeckner et al.* [2003]. The

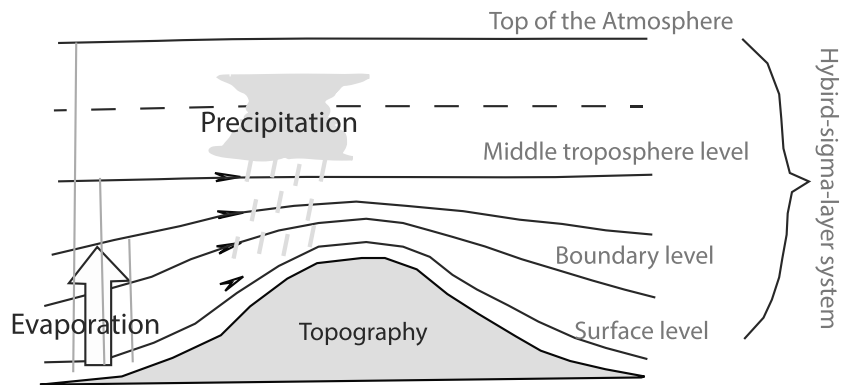


**Figure 2.** Schematic of vapor transport in the ECHAM simulation over topography and the hybrid sigma-pressure levels used in the back trajectory analysis. The precipitation is the integration of water vapor at all the atmospheric levels. It does not calculate the water budget of a target region but provides a representation of the air masses arriving that region.

ECHAM5-wiso model is an enhanced version of ECHAM5 with the added ability to simulate isotope composition in precipitation. Water isotopologues ( $\text{H}_2^{16}\text{O}$ ,  $\text{H}_2^{18}\text{O}$ , and HDO) undergo kinetic and equilibrium fractionation during the phase transitions in the atmosphere and are treated as independent tracers (for details, see Hoffmann *et al.* [1998] and Werner *et al.* [2011]). Its performance has been evaluated in several publications [Werner *et al.*, 2011; Langebroek *et al.*, 2011; Butzin *et al.*, 2014] that demonstrate agreement of the simulated isotopic fraction of precipitation with observational data on both a global scale and a regional scale. Yao *et al.* [2013] evaluated the application of different isotope tracking approaches (including ECHAM5-wiso) over the Tibetan Plateau and suggested that high-resolution atmospheric models capture the temporal and spatial distribution of  $\delta^{18}\text{O}_p$  and its relationship with vapor transport.

## 2.2. Model Setup and Boundary Conditions

An ECHAM5-wiso simulation was conducted for modern conditions at a T63 spectral resolution (equivalent to a grid spacing of  $\sim 1.9^\circ$  or  $\sim 200$  km in latitude and longitude) and L19 vertical resolution (19 vertical levels up to 10 hPa). Figure 1b shows the Tibetan Plateau topography at 1 km and T63 resolution. A comparison of these figures shows that T63 topography does not represent individual mountain ranges but rather only the long-wavelength topographic features. The simulation was forced with present-day boundary conditions including the Atmospheric Model Intercomparison Project 2 sea surface temperature and sea ice data from 1957 to 2000 and observed greenhouse gas concentrations for the same period [Nakicenovic *et al.*, 2000]. The simulation was conducted for  $>40$  model years. A climatological reference period of 30 years was established for the analysis presented here using the simulation years 1970–1999. The  $\delta^{18}\text{O}$  of soil water often requires a longer equilibrium time due to the greater heat capacity of soil and thus longer equilibrium time. Since the isotopes are not tracked on land (e.g., for soil wetness), the model spin-up time for the atmosphere and  $\delta^{18}\text{O}_p$  to equilibrate was less than 2 years.

## 2.3. Lagrangian Trajectory Analyses

Spatial variations in the water isotope fraction occur across the world [Bowen and Revenaugh, 2003]. Vapor originating from different source regions contains different isotope ratios and therefore influences  $\delta^{18}\text{O}_p$  of the target regions where precipitation occurs. However, the  $\delta^{18}\text{O}_p$  of a target region is influenced not only by the water isotopic fraction of the source region but also by other processes such as moisture convection, vapor transport distance, and the climate condition along the vapor transport path.

Lagrangian trajectory analysis is a method of defining air mass trajectories and source regions. In this study, the backward trajectories of winds that deliver precipitation are approximated in a 3-D terrain-following pressure level system referred to as hybrid sigma-pressure levels. A schematic of the hybrid sigma-pressure levels used in this study is shown in Figure 2. The hybrid sigma-pressure level approach uses a terrain-following pressure level system that enables tracking of moisture advection from below the plateau onto the Tibetan Plateau. This hybrid sigma-pressure level approach is preferred over using fixed pressure levels because of the large topographic variations between the lowlands surrounding the Tibetan Plateau and

the plateau itself. For example, a trajectory analysis conducted at a constant pressure of 900 hPa would not allow calculation of back trajectories from the plateau (at a much lower pressure) to the vapor source. Large-scale tropical convection is influenced by moisture vapor not only near the surface but also aloft [Sherwood *et al.*, 2010]. Given this, our trajectory analysis was conducted at three atmospheric levels. These levels span from the Earth's surface to 300 hPa and include (Figure 2) the following: (1) a surface level, (2) a boundary level, and (3) a middle troposphere level. The wind fields in the previous three hybrid sigma-pressure levels are integrated within each of the three levels for the calculation. The three hybrid sigma-pressure levels used in this study are composed of model hybrid sigma-pressure levels 19–11. Thus, three model levels are grouped into each of the three atmospheric levels used (Figure 2) in our back trajectory analysis. For the backward tracking, we start from one coordinate, check the average  $u$  and  $v$  wind velocities at this coordinate, and calculate where an air parcel of this target location was in the previous time increment (20 min). Following this, we determine the wind speed of the new location at that time step and track it backward one time step further, etc. This procedure was repeated until the 10 day path of the trajectory is determined.

One limitation of this approach is that it does not strictly follow water parcels or account for mixing or precipitation along a pathway. Despite this limitation, the backward trajectory technique used here provides insight into the vapor path and source of precipitation for winds in the lower troposphere in a region of high topographic variation.

A brief summary of the Lagrangian back trajectory calculation is provided here. A more detailed description is available in Bertò [2005]. A differential equation for the trajectory analysis is defined to describe the trajectory of a specific infinitesimally small air parcel:

$$\frac{dX}{dt} = X[\dot{X}(t)] \quad (1)$$

where  $t$  is time,  $X$  is the parcel position at time  $t$ , and  $\dot{X}$  is the velocity vector at time  $t$ . Using a short integration time step, the solution of equation (1) can be solved numerically to a second order:

$$X(t_1) = X(t_0) + (\Delta t) \left. \frac{dX}{dt} \right|_{t_0} + \frac{1}{2} (\Delta t)^2 \left. \frac{d^2X}{dt^2} \right|_{t_0} + \dots \quad (2)$$

The trajectories are calculated in this study using the “real-time” simulated 6 h  $u$  and  $v$  components of the wind velocity field, rather than the long-term mean wind fields from the model outputs. The 6 h wind velocity field was linearly interpolated in each pressure level to a 20 min time interval. The wind vectors at a target location inside the T63 resolution grid box were interpolated using a bilinear interpolation. The trajectories were calculated for 10 days prior to 15 January and 15 August for each of the 30 simulation years for the results presented in section 3.3. The fifteenth day was chosen because it is the midpoint of months within different seasons.

Extreme values in  $\delta^{18}\text{O}_p$  are discussed in section 4.3, and back trajectories for these were calculated for the days prior to extreme events. The wind (east-west wind and south-north wind) field of those three representative atmospheric levels is averaged from the corresponding model hybrid sigma-pressure levels and used for the trajectory calculation.

#### 2.4. Rayleigh Distillation Model (RDM) of Adiabatic Condensation

The RDM modeling approach is a simplified approach used to predict water isotope fractionation in many paleoproxy interpretation studies (e.g., Rowly and Garione [2007]). In this study we compare the RDM approach to the more sophisticated ECHAM5-wiso-predicted  $\delta^{18}\text{O}_p$  to evaluate under what conditions the RDM approach is justified. The motivation for this two-model comparison is to evaluate if the RDM (adiabatic processes) agrees with GCM predictions that account for both adiabatic and diabatic atmosphere processes. The simpler RDM calculates the condensation and change in isotopic composition of a single air parcel during adiabatic cooling. It tracks water vapor content, and the condensate isotopic fraction of a single near-surface air parcel as it ascends over topography, thereby providing the precipitation isotopic fraction as a function of elevation. In contrast, the ECHAM5-wiso GCM accounts both adiabatic and diabatic hydrological processes. Water isotopologues are allowed to undergo equilibrium and kinetic fractionation during phase changes in the atmosphere.

The RDM approach used in this study follows that of Rowley and Garzzone [2007] and Feng et al. [2013]. The RDM model is based on the conservation of moist static energy. As an unsaturated air parcel ascends, it cools at a dry adiabatic lapse rate until its temperature decreases to the dew point and then cools at the moist adiabatic lapse rate. The temperature and altitude curve can be modeled, and the remaining vapor fraction  $f$  can be calculated from the saturation vapor pressure that depends on the temperature. The delta value of remaining vapor and condensation can then be calculated as

$$(\delta^{18}\text{O}_v)_j = \left( (\delta^{18}\text{O}_v)_{j-1} + 1000 \right) f^{(\alpha-1)} - 1000 \quad (3)$$

$$(\delta^{18}\text{O}_l)_j = \alpha \left( (\delta^{18}\text{O}_v)_j + 1000 \right) - 1000 \quad (4)$$

where  $j$  is the  $j$ th elevation level,  $l$  is for the condensed vapor,  $v$  is the remaining vapor, and  $\alpha$  is the fractionation factor and can be calculated using the method of Majoube [1971] for liquid vapor equilibrium. Condensation is assumed to be equal to precipitation in the RDM.

The initial condition of the RDM calculation ( $\delta^{18}\text{O}$  in the water vapor, relative humidity, and temperature) is driven from the GCM outputs. The GCM-derived RDM initial conditions are averaged from the GCM model outputs for the monsoon season at the Himalaya front (84°E–92°E, 23°N–30°N). The RDM  $\delta^{18}\text{O}_p$  is calculated starting with a GCM-derived moisture source at low elevation (the foreland of the Himalaya). The GCM-simulated  $\delta^{18}\text{O}_p$  with elevation is then compared to the RDM prediction to evaluate the difference between the approaches over the large elevation gradient of the Himalaya.

### 2.5. Analysis of $\delta^{18}\text{O}$ Mixing

An assumption of the RDM model is that an air parcel is isolated and has no exchange with its surroundings. In reality this assumption may not always be valid. Analysis of  $\delta^{18}\text{O}$  mixing in a GCM [e.g., see Feng et al., 2013] can be used to evaluate the extent to which  $\delta^{18}\text{O}$  mixing affects  $\delta^{18}\text{O}_p$  values. Using model-estimated three-dimensional wind fields and vapor  $\delta^{18}\text{O}$  fields as inputs, the temporal difference of the  $\delta^{18}\text{O}$  of equilibrium condensate ( $\delta^{18}\text{O}_c$ ) due to flow in three directions (latitudinal, longitudinal, and vertical) can be estimated by equation (5). For this calculation, the  $\delta^{18}\text{O}_l$  in equation (4) is assumed to be the same as  $\delta^{18}\text{O}_c$  under the assumption that all condensate vapor produces precipitate.

$$\frac{\partial \delta^{18}\text{O}_c}{\partial t} \sim -\vec{V} \cdot \vec{\nabla} \delta^{18}\text{O}_v \quad (5)$$

where  $\vec{V}$  is the wind vector in the three directions. By assuming immediate condensation of advected vapor and using the fraction factor  $\alpha$  [Majoube, 1971] for liquid vapor equilibrium, the  $\delta^{18}\text{O}$  mixing rate can be calculated from

$$\vec{V} \cdot \vec{\nabla} \delta^{18}\text{O}_c = \vec{V} \cdot \vec{\nabla} \delta^{18}\text{O}_v + \vec{V} \cdot \vec{\nabla} T \left( -\frac{6.7123 \times 10^3}{T^2} + \frac{3.3328 \times 10^6}{T^3} - \frac{1.05123 \times 10^9}{T^4} \right) \quad (6)$$

The analysis of  $\delta^{18}\text{O}$  mixing provides the upper limit but not the actual value for two reasons: (1) this method assumes full condensation of the advected vapor and (2) the  $\delta^{18}\text{O}$  mixing is calculated for the monsoon season (July–September) when vapor content and precipitation amounts are the largest in the Tibetan Plateau region.

## 3. Results

In the following sections we present results for (1) model-simulated temperature, precipitation, and  $\delta^{18}\text{O}$ ; (2) spatial and temporal variations in simulated  $\delta^{18}\text{O}$ ; and (3) vapor source analyses based on the trajectory and zonal winds.

### 3.1. Model Validation and Seasonal Plots of Tibetan Plateau Temperature, Precipitation, Wind, and $\delta^{18}\text{O}_p$

The Himalaya and Tibet regions have two distinct seasons including a dry (winter) season and a wetter (summer) season. The simulated temperature and precipitation have been compared and validated with previous modeling studies and reanalysis data from across the Tibetan Plateau. The results show an agreement that is within the differences between the ERA-40 and National Centers for Environmental Prediction

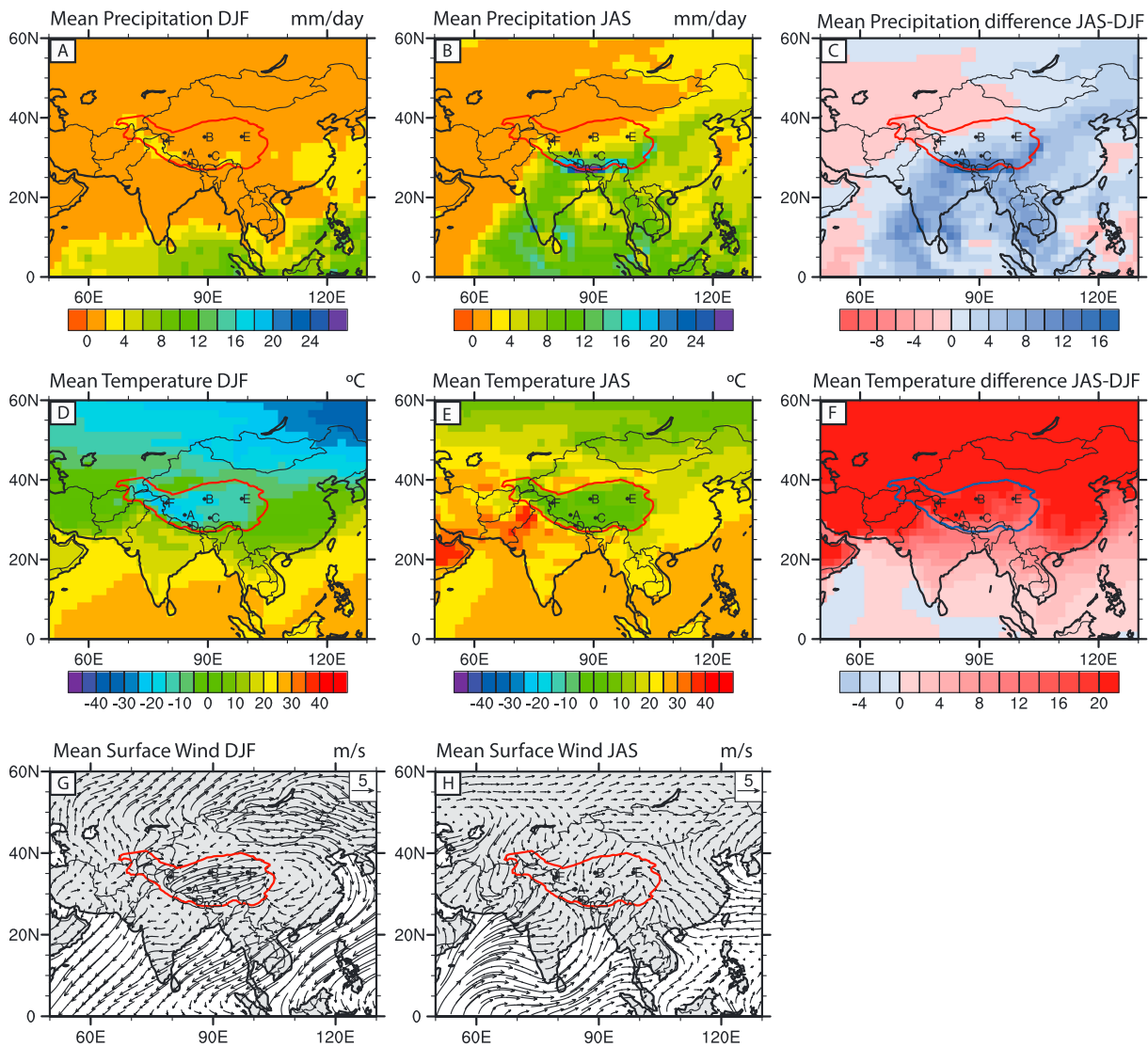


**Figure 3.** (a–c) Simulated seasonal precipitation, (d–f) surface temperature, and (g and h) surface winds for the Tibetan Plateau during winter (DJF) (Figures 3a, 3d, and 3g) and summer (JAS) (Figures 3b, 3e, and 3h), and the seasonal difference (JAS – DJF) for precipitation and temperature (Figures 3c and 3f). The contour line marks the region where the topography exceeds 1500 m elevation.

reanalysis data. This comparison is presented in *Mutz et al.* [2016] using the same resolution ECHAM5-wiso model outputs as this study. Thus, the model resolution used in this study agrees with reanalysis data and the different reanalysis data sets agree with each other [*Mutz et al.*, 2016]. Furthermore, our study uses a T63 resolution ECHAM5 model. A lower resolution (T42) version of ECHAM has already been used and validated for climate studies [*Battisti et al.*, 2014; *Roe et al.*, 2016]. More specifically, *Battisti et al.* [2014] provide a comparison of simulated and observed precipitation and also report a good agreement with stalagmite proxy records. *Roe et al.* [2016] conducted a limited set of simulations at higher resolution but found no significant differences from the lower resolution analysis. Finally, *Werner et al.* [2011] and *Yao et al.* [2013] suggested that a higher model resolution provides better results on smaller scale (mainly due to a better resolved topography) but does not result in large changes of the general temperature, precipitation, and  $\delta^{18}O_p$  patterns such as we interpret from the model results in this manuscript.

Figure 3 shows the 30 year climatologies of the winter (defined as December-January-February, DJF) and summer (defined as July-August-September, JAS) seasons and the difference between summer and winter seasons (JAS – DJF). In the winter, there is small amount (<4 mm/d) of precipitation across the Tibetan

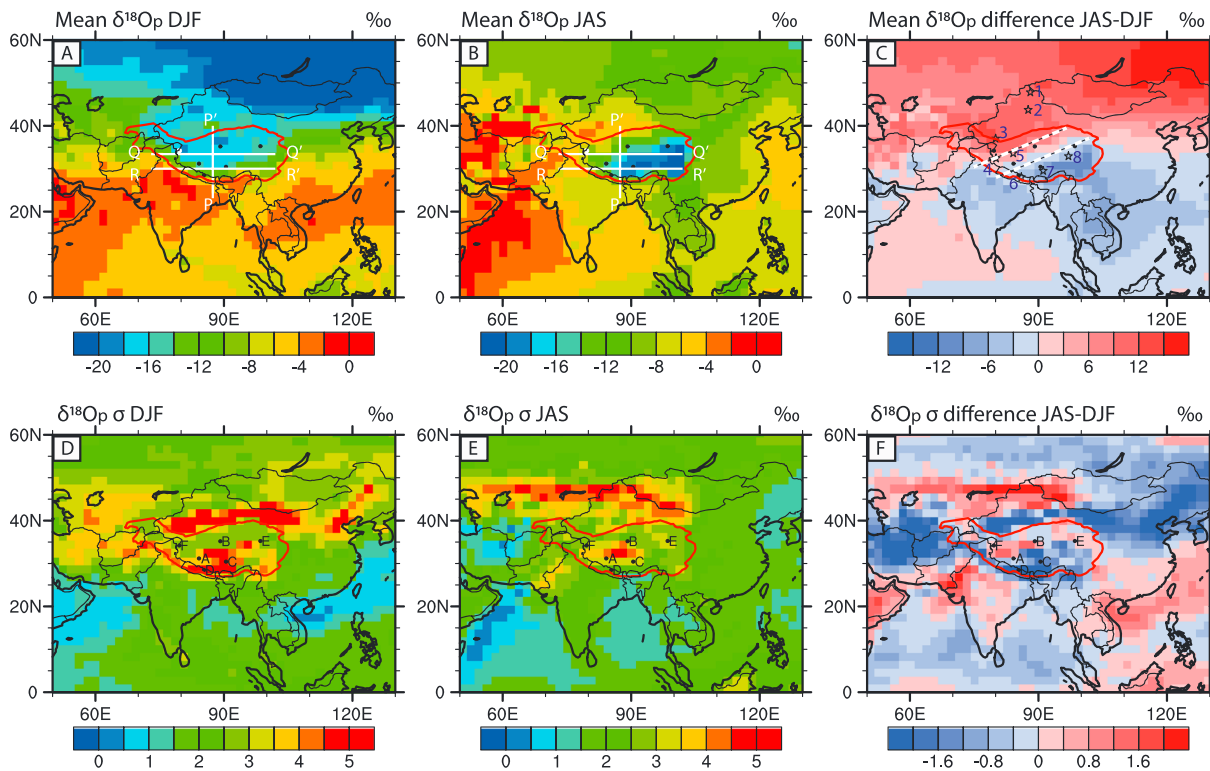


**Figure 4.** Simulated (a and d) DJF, (b and e) JAS, and (c and f) the seasonal difference (JAS – DJF) for the precipitation-weighted mean  $\delta^{18}\text{O}_p$  (Figures 4a–4c) and its standard deviation ( $\sigma$ ) (Figures 4d–4f) for the Tibetan Plateau. White lines in Figures 4a and 4b represent the analyzed  $\delta^{18}\text{O}_p$  cross sections shown in Figures 8 and 12, longitude of the north-south cross section P–P' at 87.5°E, latitude of the west-east cross section Q–Q' at 33°N, and latitude of the second west-east cross section R–R' at 30°N. The white dash lines in Figure 4c illustrate the separation of the three  $\delta^{18}\text{O}_p$  distribution zones. Numbers in Figure 4c represent the observational data locations we compared in Figure 11. The locations represented by number are 1 (Altay), 2 (Urumqi), 3 (Hetian), 4 (Shiquanhe), 5 (Gaize), 6 (Nyatam), 7 (Lasha), and 8 (Yushu). Black dots with letters in Figures 4d–4f represent the locations where bar-whisker plots in Figures 5–7 are from and the locations used for trajectory analysis shown in Figures 9, 10, and 13. Those locations are A (Taro Co: 31.18°N, 84.17°E), B (Qang Co: 35.19°N, 89.15°E), C (Nam Co: 30.44°N, 90.47°E), D (Paiku Co: 28.49°N, 85.35°E), and E (Donggi Cona: 35.25°N, 98.5°E).

Plateau (Figure 3a). In summer (Figure 3b) precipitation rates are  $<4$  mm/d in NW Tibet but significantly higher over the Himalaya ( $\sim 20$  mm/d) and most of the SE Plateau ( $\sim 10$  mm/d). There is less precipitation (0–4 mm/d) in NW Tibet but more precipitation (increasing from 0 to 4 mm/d in the middle of Tibet to  $>10$  mm/d over SE Tibet) in the summer than in winter (Figure 3c). The mean surface temperature is about  $-25^\circ\text{C}$  in NW Tibet and  $-15^\circ\text{C}$  in SE Tibet in the winter (Figure 3d) and increases to around  $0^\circ\text{C}$  across Tibet in the summer (Figure 3e). The mean summer and winter temperature difference increases from south to north across Tibet from around  $0^\circ\text{C}$  to  $20^\circ\text{C}$  (Figure 3f). Analysis of the seasonality of the Tibetan Plateau surface winds also illustrates two distinct patterns. Strong westerly winds prevail in the winter (Figure 3g). In summer, southeasterly winds associated with the Indian monsoon system arrive in the Himalaya (Figure 3h).

Summer and winter differences in  $\delta^{18}\text{O}_p$  (precipitation-weighted mean) is also present. In the winter, spatial variations in  $\delta^{18}\text{O}_p$  are  $\sim 5\text{‰}$  over the Tibetan Plateau (Figure 4a), whereas in the summer, the  $\delta^{18}\text{O}_p$  distribution shows a distinct northwest-southeast spatial gradient decreasing from  $\sim -5\text{‰}$  in NW Tibet to  $\sim -20\text{‰}$  in SE Tibet (Figure 4b). The seasonal difference (JAS – DJF) in  $\delta^{18}\text{O}_p$  is  $>+6\text{‰}$  in the NW Tibetan Plateau and  $<-6\text{‰}$  in the SE Tibetan Plateau (Figure 4c). Different from the zonal distributions in  $\delta^{18}\text{O}_p$  that are observed in previous studies [e.g., Tian et al., 1997; Yao et al., 2013], the three zones extend from the SE to the NW (as indicated with white dash lines in Figure 4c), rather than from south to north. This information is important for paleoclimatology and paleoaltimetry studies when interpolating proxy data for the Tibetan Plateau. This SE to the NW direction of  $\delta^{18}\text{O}_p$  zones and the climate controls on it have been independent of this study identified by a cluster analysis of  $\delta^{18}\text{O}_p$  [Mutz et al., 2016]. The standard deviation ( $\sigma$ ) in  $\delta^{18}\text{O}_p$  was calculated from 90 monthly means of predicted  $\delta^{18}\text{O}_p$  (30 simulation years  $\times$  3 month in a season). The winter  $\sigma$  in  $\delta^{18}\text{O}_p$  values vary between  $\sim 2$  and  $4.5\text{‰}$  in south central Tibet (Figure 4d). The  $\sigma$  of summer  $\delta^{18}\text{O}_p$  is  $\sim 2$  to  $4.5\text{‰}$  in

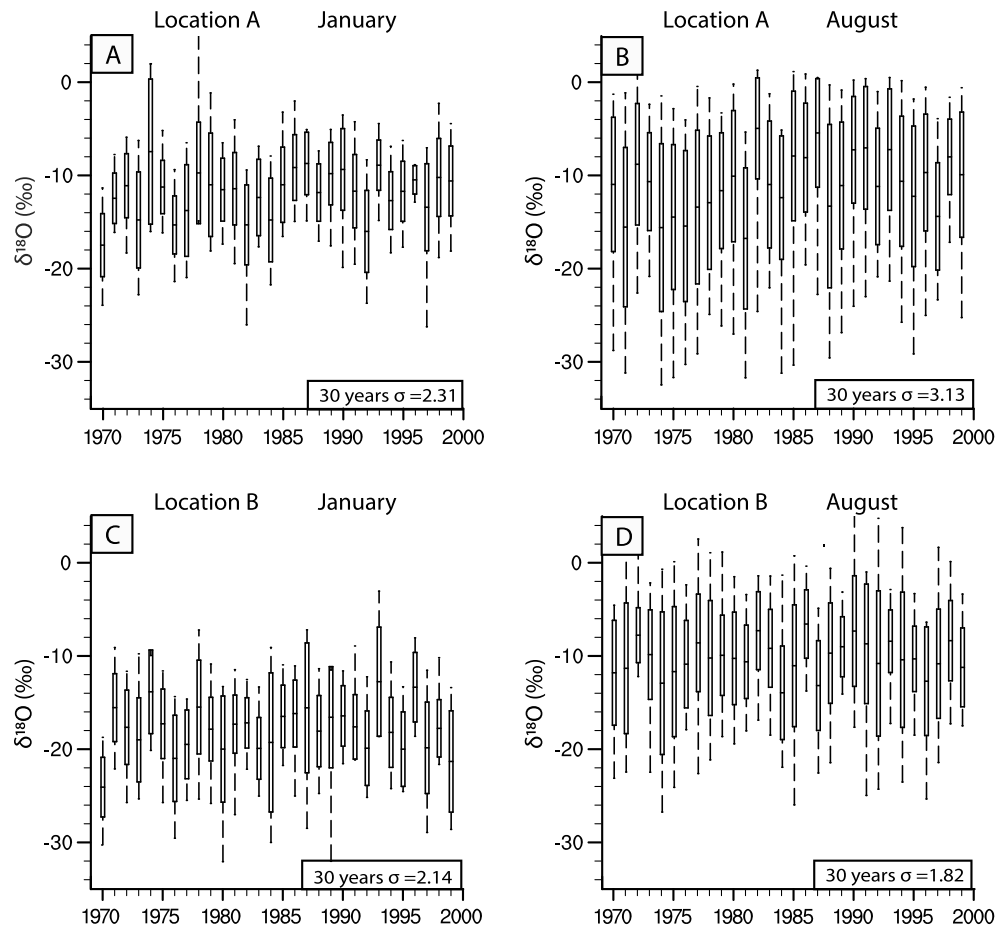


**Figure 5.** (a and c) January and (b and d) August  $\delta^{18}\text{O}_p$  distribution at location A (Figures 5a and 5b) and the location B (Figures 5c and 5d) in the middle zone. Maximum, mean +  $1\sigma$ , mean, mean -  $1\sigma$ , and minimum of the daily  $\delta^{18}\text{O}_p$  values are shown in the box plots. Seasonal trends show low  $\delta^{18}\text{O}_p$  in winter and high  $\delta^{18}\text{O}_p$  in summer, and the seasonal difference in  $\delta^{18}\text{O}_p$  is  $\sim 10\text{‰}$ .

central Tibet (Figure 4e). The summer-winter difference (JAS - DJF) in the  $\sigma$  of  $\delta^{18}\text{O}_p$  is most positive in northern Tibet and most negative in southern Tibet (Figure 4f). In the following sections we simplify our presentation by focusing on January and August as representative months for the winter and summer. These months were selected for the back trajectory analysis which requires high-resolution (20 min) wind velocities.

### 3.2. Thirty Year Spatial and Temporal Variations in $\delta^{18}\text{O}$

Spatial and temporal variations in  $\delta^{18}\text{O}_p$  are presented for two profiles across the Tibetan Plateau (white lines in Figures 4a and 4b) and for six selected locations (black dots and letters in Figures 4d and 4e which represent cities, significant geographic features such as lakes, or published proxy data sample locations). In this section, we focus on a statistical analysis of the daily time series for the six selected locations: location A and B from the middle transition zone; location C, D, and E from the southeast zone, and location F from the northwest zone (Figure 4d). The environmental controls of  $\delta^{18}\text{O}_p$  are discussed in section 4.

Strong variations in mean daily  $\delta^{18}\text{O}_p$  are observed in January and August over the 30 year simulation duration in all six selected locations on the Tibetan Plateau (Figures 5-7). In these figures, monthly values are presented and include the maximum and minimum daily  $\delta^{18}\text{O}_p$ , mean daily  $\delta^{18}\text{O}_p$  (dashed lines), and  $\pm 1\sigma$  (standard deviation) from the mean  $\delta^{18}\text{O}_p$  value (boxes). Two general patterns are evident. First, large variations in the daily mean  $\delta^{18}\text{O}_p$  are present and range from  $\sim -25$  to  $+5\text{‰}$ . These daily variations agree well with the results of Liu et al. [2010] that reported a daily variation of  $-28.7\text{‰}$  to  $-7.8\text{‰}$  based on 70 daily measurements of  $\delta^{18}\text{O}_p$  in the year 2000 at Nague ( $31.48^\circ\text{N}$ ,  $92.06^\circ\text{E}$ ) in the central Tibetan Plateau. Second, large

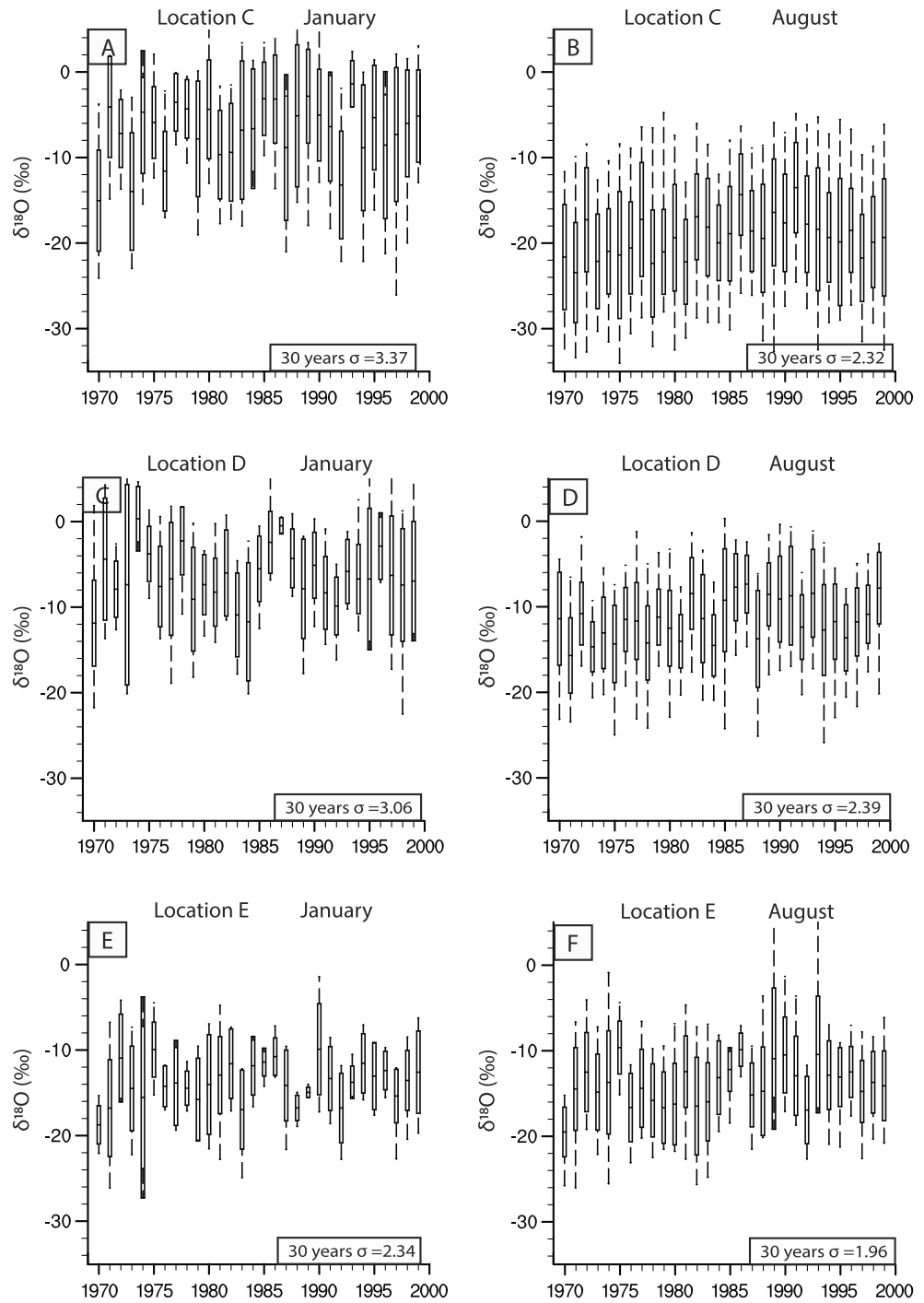


**Figure 6.** (a, c, and e) January and (b, d, and f) August  $\delta^{18}\text{O}_p$  distribution at location C (Figures 6a and 6b), location D (Figures 6c and 6d) and location E (Figures 6e and 6f) in the southeast zone. Labels are the same as in Figure 5. A similar seasonal trend in  $\delta^{18}\text{O}_p$  (low in winter and high in summer) is presented as in Figure 5 but with a smaller seasonal difference of  $\sim 0\text{‰}$ – $5\text{‰}$ .

interannual variations are also present for each area; the standard deviation of the 30 year precipitation-weighted annual  $\delta^{18}\text{O}_p$  data is about 1.2–3.5‰ for all sites.

The different regions on the Tibetan Plateau demonstrate different seasonal trends in  $\delta^{18}\text{O}_p$ . In the middle zone of the Tibetan Plateau (locations A and B; Figures 4b and 5), low mean monthly  $\delta^{18}\text{O}_p$  ( $\sim -15\text{‰}$ ) is present in the winter (Figures 5a and 5c) and higher  $\delta^{18}\text{O}_p$  ( $\sim -10\text{‰}$ ) is found in summer (Figures 5b and 5d).

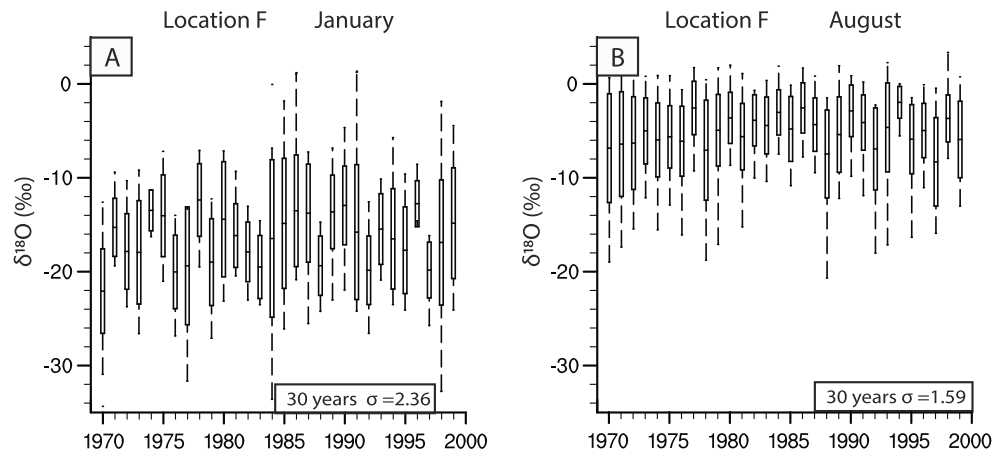


**Figure 7.** (a) January and (b) August  $\delta^{18}\text{O}_p$  distribution at location F in the northwest zone. Labels are the same as in Figure 5. Opposite  $\delta^{18}\text{O}_p$  seasonal trends are observed in this zone as in Figure 5. High  $\delta^{18}\text{O}_p$  is present in the winter and low  $\delta^{18}\text{O}_p$  present in the summer with the seasonal difference of  $\sim 2\text{‰}$ – $15\text{‰}$  at different locations.

However, the seasonal differences in mean monthly  $\delta^{18}\text{O}_p$  at each location are  $5\text{‰}$  (Figures 5a and 5b and 5c and 5d). Daily  $\delta^{18}\text{O}_p$  variations in the middle zone are much higher in the summer than in winter.

In the southeast zone (locations C, D, and E, Figures 4b and 6), there is more precipitation than the other zones due to the stronger influence of the monsoon system (Figures 3a and 3b). The different precipitation distribution in this zone results in the  $\delta^{18}\text{O}_p$  having an opposite seasonality to that of the other zones. More specifically, the precipitation events in the southeast zone (Figure 6) have higher  $\delta^{18}\text{O}_p$  in the winter and lower  $\delta^{18}\text{O}_p$  in the summer compared to the other zones (Figures 5 and 7). This trend could be caused by the high summer rainout amount. The seasonality of  $\delta^{18}\text{O}_p$  across the southeast zone varies from  $10\text{‰}$  at location C (Figures 6a and 6b) to  $3\text{‰}$  at location E (Figures 6e and 6f).

At location F, the mean daily  $\delta^{18}\text{O}_p$  is about  $-16\text{‰}$  in the winter and about  $-5\text{‰}$  in the summer (Figure 7). High  $\delta^{18}\text{O}_p$  in summer and low  $\delta^{18}\text{O}_p$  in winter are correlated with the high temperature in summer and low temperature in winter, which reflects a “temperature effect” influence on the  $\delta^{18}\text{O}_p$  variation.

North-south and west-east variations in  $\delta^{18}\text{O}_p$  are presented along two profiles in Figure 8. The following points are evident. First, seasonal differences in the spatial distribution of  $\delta^{18}\text{O}_p$  are present. For example,  $\delta^{18}\text{O}_p$  values have a lower spatial variation ( $\pm 5\text{‰}$ ) in the winter on the Tibetan Plateau (Figures 8a–8c), but a large spatial difference ( $\pm 10\text{‰}$ ) is seen in the August  $\delta^{18}\text{O}_p$  values (Figures 8d–8f). Second, minimum  $\delta^{18}\text{O}_p$  occurs at different locations on the plateau for each season. The north-south cross section (Figures 8b and 8e) indicates that the minimum in  $\delta^{18}\text{O}_p$  ( $\sim -19\text{‰}$ ) is found on the north of the Tibetan Plateau in January (Figure 8b) and migrates to the south of the Tibetan Plateau in August ( $\sim -20\text{‰}$ ) (Figure 8e). The west-east cross section also shows a season shift in  $\delta^{18}\text{O}_p$  values (Figures 8c and 8f). Minimum  $\delta^{18}\text{O}_p$  occurs on the west side of the Tibetan Plateau in January ( $\sim -17\text{‰}$ ) (Figure 8c) and migrates to the east in August ( $\sim -20\text{‰}$ ) (Figure 8f). Third, similar  $\delta^{18}\text{O}_p$  and isotopic lapse rates of  $\sim -3.1\text{‰}/\text{km}$  are present in the Himalaya and southern Tibetan Plateau for both seasons (Figures 8b and 8e). In contrast, the western side of the Tibetan Plateau has a lapse rate of  $\sim -3.4\text{‰}/\text{km}$  in the winter (Figure 8c) that decreases to  $-1.7\text{‰}/\text{km}$  in the summer (Figure 8f). These results indicate that seasonal variations in  $\delta^{18}\text{O}_p$  are present but spatially variable in their magnitude across the Himalaya and Tibetan Plateau.

### 3.3. Vapor Source Analysis Based on Trajectory Analysis

Results from the Lagrangian trajectory analysis are presented here to assess how seasonal variations in the vapor source influence predicted  $\delta^{18}\text{O}_p$  values. Trajectories were computed for 10 days prior to 15 January and 15 August of the 30 simulation years (Figures 9 and 10). Location F in the northeast and location C in the southeast are presented as representative examples for vapor transport at the three hybrid sigma-pressure levels (section 2.3 and Figure 2, surface level, boundary level, and middle troposphere level). Trajectories show localized circulation at the surface layer which represents an inversion that would tend

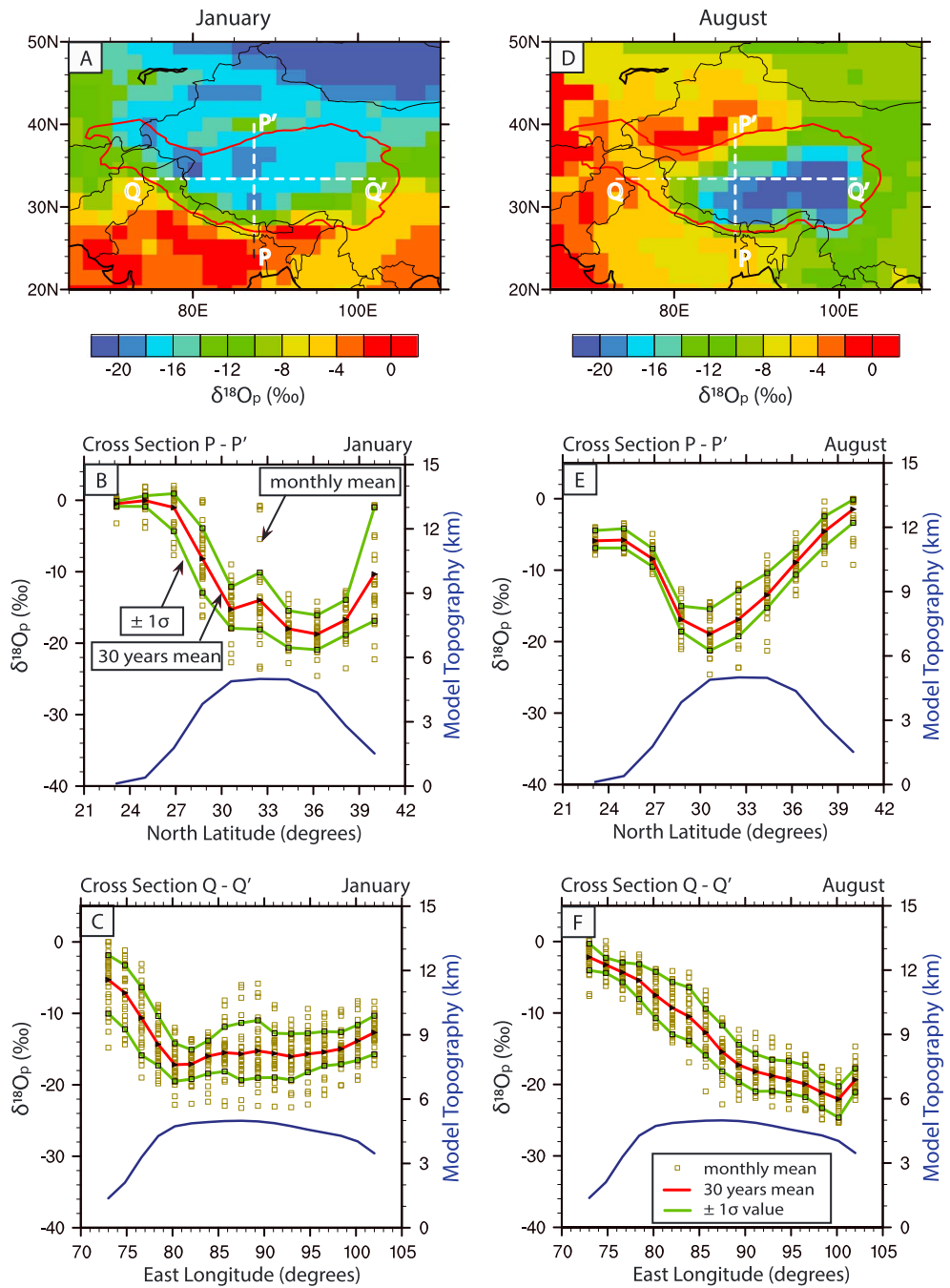


**Figure 8.** Contour map of (a and d)  $\delta^{18}O_p$  and (b and e) west-east (cross section P-P' at 33°N) and (c and f) north-south (cross section Q-Q' at 87.5°E)  $\delta^{18}O_p$  profiles for January (Figures 8a–8c) and August (Figures 8d–8f). Red line in contour maps marks the region where the topography exceeds 1500 m. Red lines in cross-section profiles represent the long-term mean  $\delta^{18}O_p$  value. Green lines represent  $\pm 1\sigma$  value of long-term  $\delta^{18}O_p$ . Squares show the monthly mean of  $\delta^{18}O_p$  for 30 simulation years. Blue lines show the topography cross-section profiles.

to prevent strong mixing from aloft and a prevailing westerly pathway in the boundary layer and midtroposphere in January (Figure 9). The trajectories for these locations track predominantly westerly winds from the western arid region to the Tibetan Plateau.

August trajectories for the same locations on the Tibetan Plateau show a different pattern than for January (Figure 10). Location C is strongly influenced by the monsoon system in August (Figures 10e and 10f) such that most vapor originates from the Indian Ocean. In contrast, vapor at location F is more heavily influenced

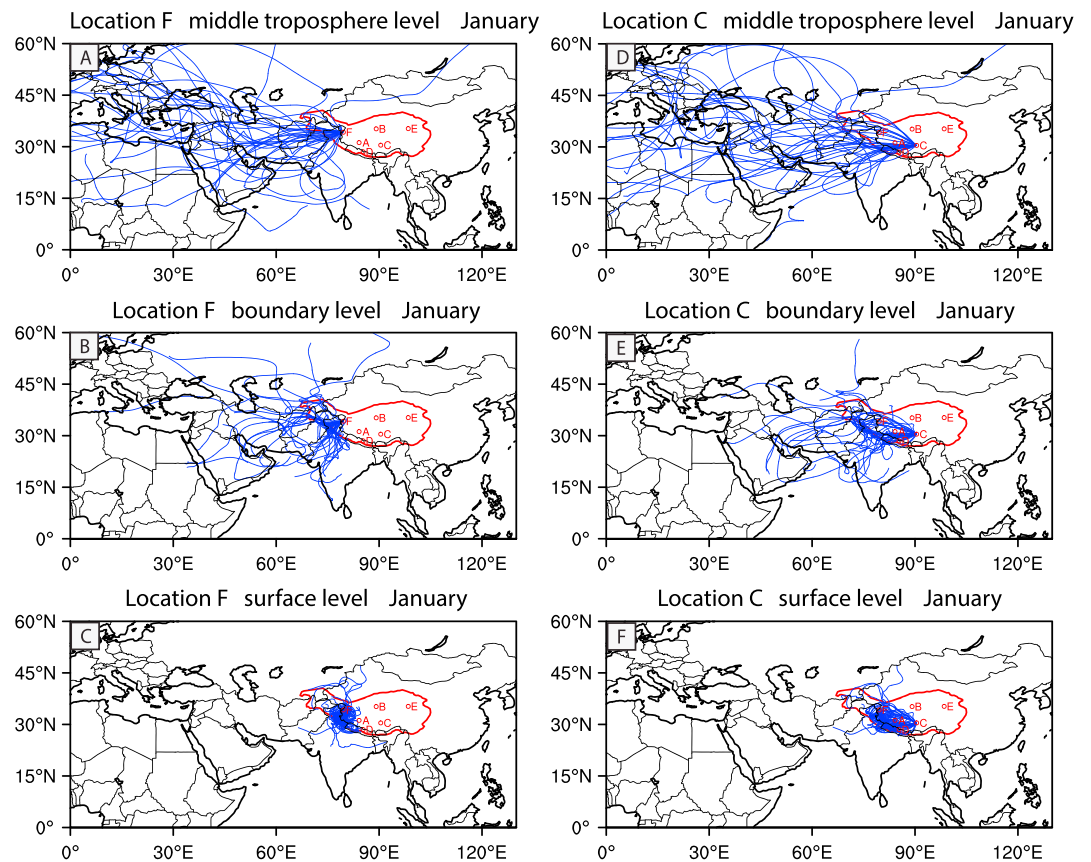


**Figure 9.** Calculated January backward trajectories at three atmosphere levels: (a and d) middle troposphere level, (b and e) boundary level, and (c and f) surface level at location F (Figures 9a–9c) in the northwest zone and location C (Figures 9d–9f) in the southeast zone. The trajectories are backward tracked for 10 days.

by the westerlies and back trajectories lead to either the NW or SW of the Tibetan Plateau (Figure 10c). A second prominent feature of the rainy season is that dry air is sourced from the west in the middle troposphere (Figure 10d). These results are consistent with those of *Hren et al.* [2009], who found that the monsoon-derived moisture is progressively mixed with central Asian air masses in the western and northern parts of the Tibetan Plateau.

#### 4. Discussion

In the following sections we discuss the results in the context of (1) a comparison of GCM predictions and observations (precipitation and stream water  $\delta^{18}\text{O}$ ), (2) the causes for the extreme values in  $\delta^{18}\text{O}$ , and (3) application of the RDM at the Himalayan front.

##### 4.1. Predicted and Observed Precipitation $\delta^{18}\text{O}$ Comparison

The performance of the ECHAM5-wiso-predicted 30 year average  $\delta^{18}\text{O}_p$  is compared to observations to evaluate the model performance. Two years of observational  $\delta^{18}\text{O}_p$  data were available for comparison from *Tian et al.* [2007]. A 30 year model-predicted average  $\delta^{18}\text{O}_p$  was compared to individual years of observations to assess if the individual observations occur within the range of model-predicted values. The locations of observed  $\delta^{18}\text{O}_p$  studies are shown in Figure 4c, and individual station locations were compared to simulations using a bilinear interpolation of model grid cells to each location (Figure 11). Overall, a good agreement is present between predicted and observed values. Model predictions successfully produce seasonal variations in  $\delta^{18}\text{O}_p$  at several locations (e.g., Figures 11a, 11b, and 11f–11h). However, differences between predicted and observed values are present. Large ( $>2\sigma$  of the model 30 year outputs) differences between the model and observation are found at Shiquanhe and Yushu (Figures 11c and 11e). For example, the model

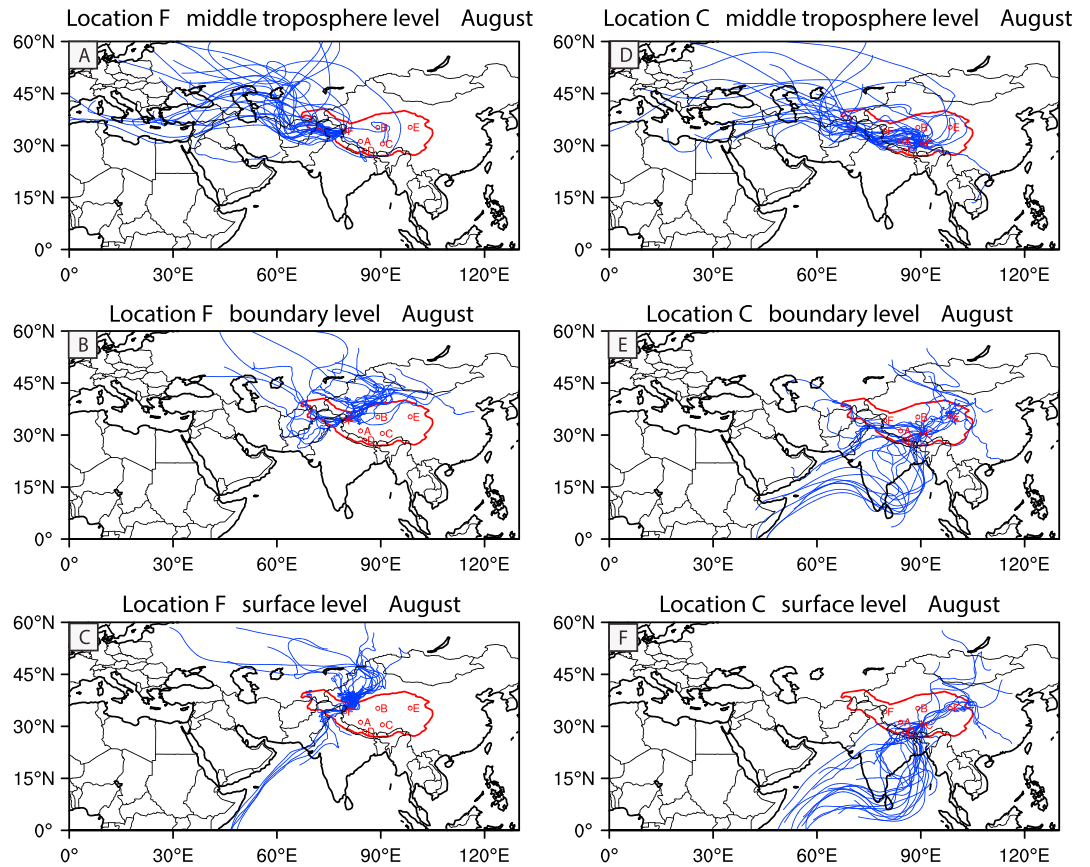


**Figure 10.** Calculated August backward trajectories at three atmosphere levels: (a and d) middle troposphere level, (b and e) boundary level, and (c and f) surface level at the location F (Figures 10a–10c) in the northwest zone and at the location C (Figures 10d–10f) in the southeast zone. The trajectories are backward tracked for 10 days.

$\delta^{18}\text{O}_p$  prediction for the northwestern Tibetan Plateau is higher than observations during the winter and spring (Figures 11c, 11d, and 11f–11h). These differences could result from several factors. First, the differences might suggest an influence of topographic effects on  $\delta^{18}\text{O}_p$  at Shiquanhe and Yushu that are not present in the model due to its resolution. Second, there is a model bias of overestimating of  $\delta^{18}\text{O}_p$  during the winter in the westerly region. And third, the 2 years of  $\delta^{18}\text{O}_p$  observational data used in this comparison deviate by two to three standard deviations from the 30 year climatological averages thereby allowing for the possibility that extreme variations from the mean were measured in those years (Figures 11c–11e). More observations from these locations are needed to differentiate between the above explanations.

**4.2. Predicted and Observed Stream Water  $\delta^{18}\text{O}$  Comparison**

Previous work by Hren *et al.* [2009] presented  $\delta^{18}\text{O}$  from stream waters ( $\delta^{18}\text{O}_{\text{water}}$ ) at  $\sim 30^\circ\text{N}$  and  $\sim 86^\circ\text{E}$  that were intermittently measured from 1998 to 1999. Stream water can reflect mean annual precipitation-weighted variations in  $\delta^{18}\text{O}_p$  [Yurtsever and Gat, 1981] and motivates presentation of the GCM-predicted mean annual  $\delta^{18}\text{O}_p$  (Figure 12). Simulated  $\delta^{18}\text{O}_p$  was plotted at the same observational cross section (Figures 12c and 12d). Simulated and observed  $\delta^{18}\text{O}$  agree well along both the west-east cross section R-R' (Figure 12c) and the north-south cross section P-P' (Figure 12d). The north-south cross section shows that  $\delta^{18}\text{O}_p$  decreases from south to north across the Himalaya and increases on the Tibetan Plateau from south to north (Figure 12d; see also August results in Figure 8e). ECHAM5-wiso  $\delta^{18}\text{O}_p$  is higher than the  $\delta^{18}\text{O}_{\text{water}}$  at the west end of Himalaya by about 4‰. Although this difference is comparable to the model-simulated interannual variability of  $\sim 4\text{--}6\text{‰}$  (Figure 12), the observations at the west end of the Himalaya are more negative than the model-predicted values. Possible causes for the remaining disagreement could include the following: (1) there is a mixing of surface waters with more isotopically depleted sources such as a stream

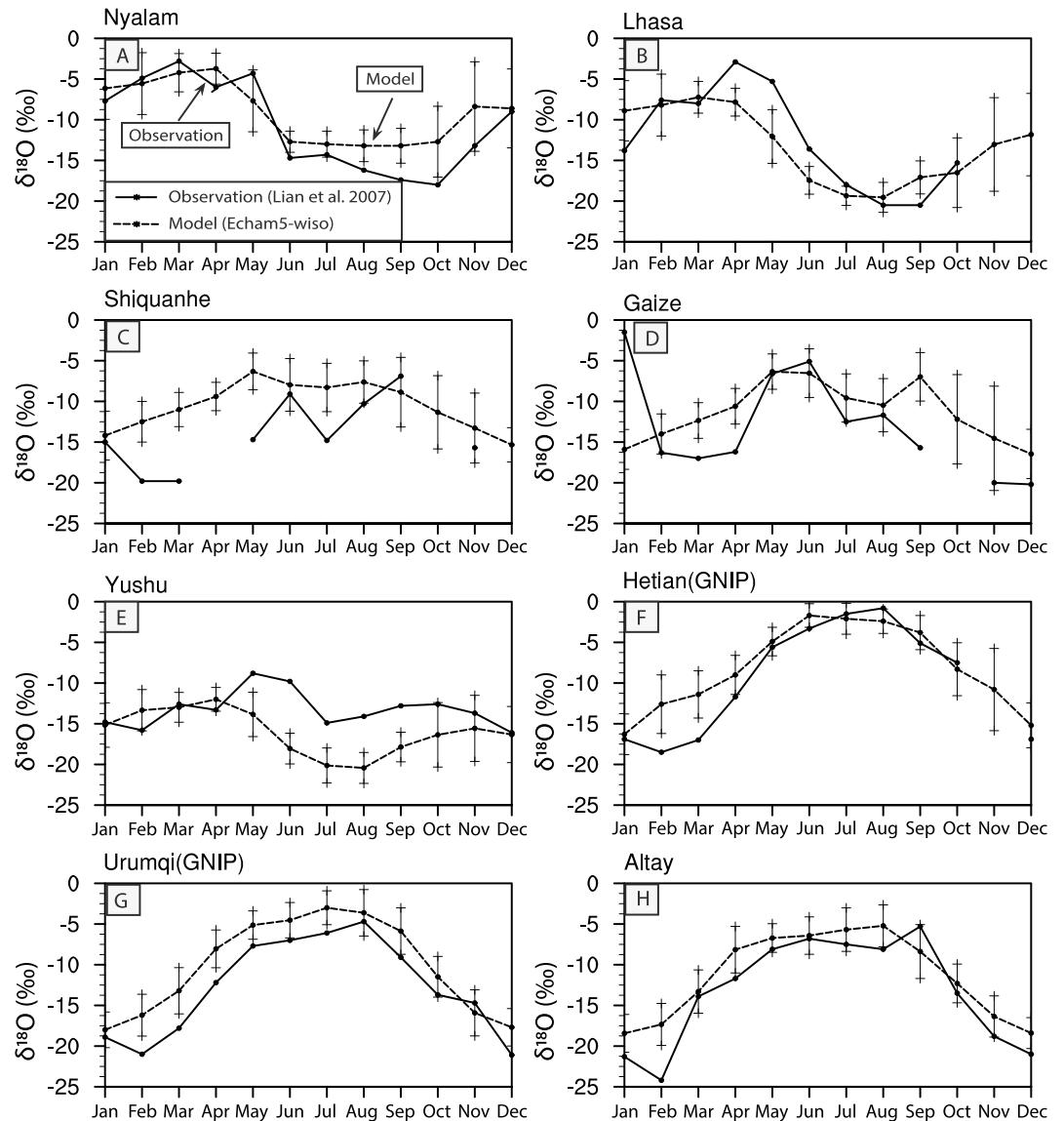


**Figure 11.** Simulated (dash line)  $\delta^{18}O_p$  and observational (solid line)  $\delta^{18}O_p$  [Tian *et al.*, 2007] comparison. The error bar of the simulated  $\delta^{18}O_p$  represents the  $\pm 1\sigma$  value.

source from a higher altitude that flows down to the sample site; (2) the west-east  $\delta^{18}O_{\text{water}}$  at the west of the Himalaya represents a local signal influenced by the catchment topography that cannot be reproduced by the GCM due to the coarser model resolution (e.g., Figure 1); (3) the observational duration of Hren *et al.* [2009] is relatively short (1 year) compared to the 30 year climatological values predicted; and (4) a systematic west to east bias in model predictions. Concerning the last point, comparisons of model results to other  $\delta^{18}O_p$  data (see section 4.1) are in agreement and suggest that the first three points are the more likely explanation.

**4.3. Causes for Extreme Values in  $\delta^{18}O_p$**

Our results indicate that the range of daily  $\delta^{18}O_p$  values is as large as 25–30‰ (Figures 5–7) [see also Liu *et al.*, 2010]. To investigate possible explanations for the range of daily  $\delta^{18}O_p$  values in the 30 simulation years (total number of days analyzed = 30 years  $\times$  31 days = 930) for each month are characterized into three groups: (1) days with extreme highs in  $\delta^{18}O_p$  values (daily value > 95 percentile of the  $\delta^{18}O_p$ ), (2) days with extreme low  $\delta^{18}O_p$  values (daily value < 5 percentile of the  $\delta^{18}O_p$ ), and (3) days with mean  $\delta^{18}O_p$  values (average  $\delta^{18}O_p$  value  $\pm 0.5\text{‰}$ ) as a reference. The conditions (temperature, precipitation, and vapor sources) of those days in the three groups are analyzed for January and August at representative locations.

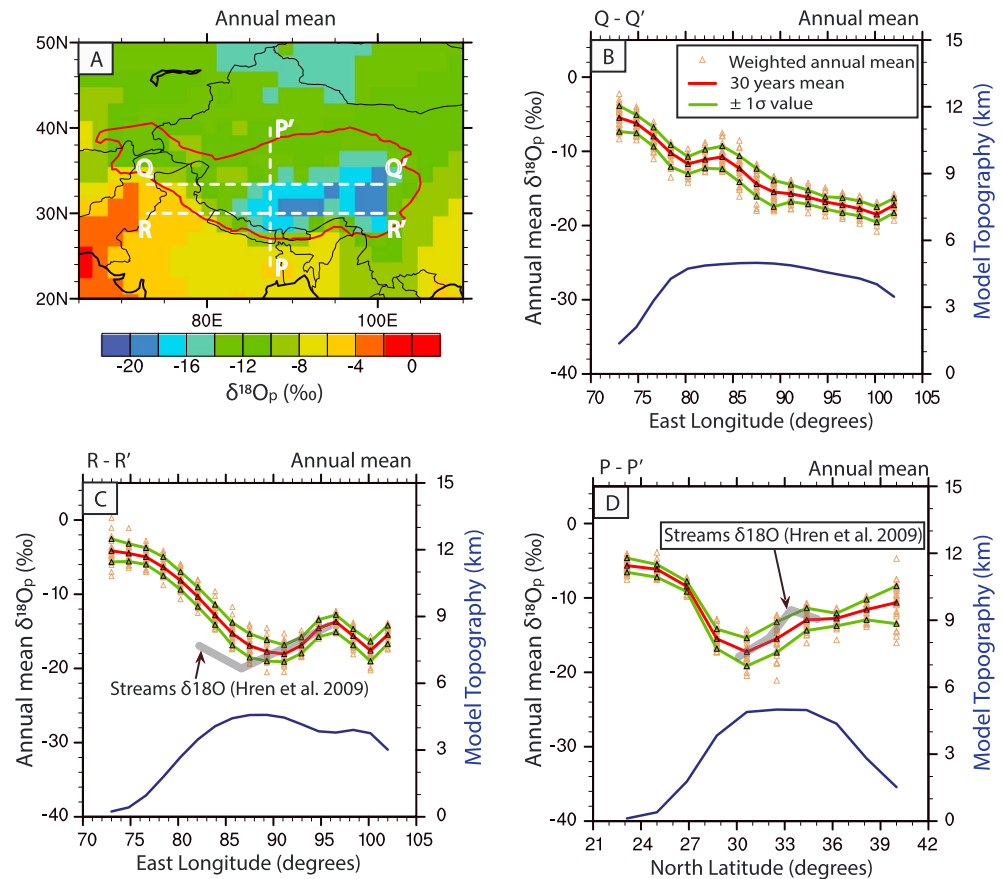


**Figure 12.** (a) Annual mean  $\delta^{18}O_p$  contour map and three  $\delta^{18}O_p$  cross-section profiles at (b) north-south cross section Q-Q', (c) west-east cross section R-R', and (d) west-east cross section P-P'. Labels are the same as in Figure 8. Grey lines show the observational stream water  $\delta^{18}O$  value published in Hren et al. [2009]. Triangles show the precipitation-weighted mean annual (abbreviated to mean annual afterward)  $\delta^{18}O_p$  for the 30 simulation years. Red lines and green lines in cross-section profiles represent the mean and  $\pm 1\sigma$  value of the 30 year mean annual  $\delta^{18}O_p$ .

The average temperature and precipitation for the three groups and their standard deviations are summarized in Table 1. An increase in the precipitation amount corresponds with a decrease in  $\delta^{18}O_p$  at most of the locations for both January and August, but there is no systematic correlation between the changes in  $\delta^{18}O_p$  and changes in the precipitation amount. For example, daily extreme precipitation ranges from 6.9 mm/d in January to 54.5 mm/d at location D during August, corresponding to values for  $\delta^{18}O_p$  of  $-2.0\text{‰}$  and  $-21.5\text{‰}$ . In contrast, daily extreme precipitation range from 0.57 to 2.78 mm/d at location F during January, corresponding to values for  $\delta^{18}O_p$  of  $-6.2\text{‰}$  and  $-30.0\text{‰}$ . We find that the temperature differences between the groups are small, with a maximum of 3°C and minimum of 0.1°C between the days with extreme high  $\delta^{18}O_p$  values and extreme low  $\delta^{18}O_p$  values. For the three groups, there is no significant correlation between temperature and  $\delta^{18}O_p$ . Finally, large daily variations in temperature and precipitation exist within the same extreme  $\delta^{18}O_p$  group. Extreme  $\delta^{18}O_p$  values do not systematically correspond with either precipitation or temperature extremes.

Apart from temperature and precipitation, vapor source can also significantly influence  $\delta^{18}O_p$ . Backward trajectory analyses were conducted to determine changes in the vapor source for the extreme event days in the above three groups at location C and location F during the months of January and August (Figure 13). Orange, blue, and green lines in Figure 13 represent backward trajectories for days with extreme high, mean, and extreme low  $\delta^{18}O_p$  values. The surface layer is not relevant for diagnosing the vapor sources outside the Tibetan region in January for the northwest region of the Tibetan Plateau (Figure 9). Given this, the surface layer trajectories for January are not shown here. Results show a clear vapor source variance for the extreme events (Figure 13). For example, at location C during August the northeast and southwest vapor sources (orange color) correspond with the extreme high  $\delta^{18}O_p$  values,

**Table 1.** The Average and Standard Deviation of Temperature, Precipitation, and  $\delta^{18}\text{O}_p$  for Days With Extreme Low  $\delta^{18}\text{O}_p$  Value, Mean  $\delta^{18}\text{O}_p$  Value, and Extreme  $\delta^{18}\text{O}_p$  Value at Six Locations for January and August, Analyzed From Model Daily Outputs of 30 Simulation Years. Bold numbers in Table 1 demonstrates the non-systematic correlation between the changes in  $\delta^{18}\text{O}_p$  and changes in the precipitation amount<sup>a</sup>

Zone	Location	$\delta^{18}\text{O}_p$ Daily Percentile	January			August		
			$\delta^{18}\text{O}_p$ ( $\sigma$ ) (‰)	$T$ ( $\sigma$ ) (°C)	$P$ ( $\sigma$ ) (mm/d)	$\delta^{18}\text{O}_p$ ( $\sigma$ ) (‰)	$T$ ( $\sigma$ ) (°C)	$P$ ( $\sigma$ ) (mm/d)
NW	F	>95%	<b>-6.23</b> (1.92)	-24.03 (4.23)	<b>0.57</b> (0.57)	0.68 (0.72)	0.55 (1.54)	0.42 (0.64)
		= Mean	-16.71 (0.29)	-22.51 (4.05)	2.21 (2.00)	-5.30 (0.27)	0.39 (1.29)	2.23 (1.83)
		<05%	<b>-29.90</b> (2.57)	-22.53 (5.03)	<b>2.78</b> (2.10)	-16.08 (1.88)	0.63 (1.28)	3.32 (3.23)
Middle	A	>95%	-2.92 (3.40)	-21.46 (5.49)	0.20 (0.28)	-0.16 (0.60)	2.10 (1.37)	1.41 (2.32)
		= Mean	-11.72 (0.30)	-21.62 (4.90)	1.23 (1.52)	-9.90 (0.30)	1.98 (1.37)	5.91 (5.32)
		<05%	-21.64 (1.93)	-18.44 (4.68)	3.64 (3.43)	-28.2 (1.95)	2.22 (1.12)	16.32 (5.88)
	B	>95%	-8.57 (2.37)	-19.88 (2.72)	0.35 (0.26)	-0.64 (2.17)	0.50 (2.0)	0.98 (1.23)
		= Mean	-18.14 (0.28)	-19.80 (2.53)	0.81 (0.63)	-10.00 (0.30)	1.08 (1.86)	3.49 (3.73)
		<05%	-27.33 (1.85)	-21.19 (3.12)	0.65 (0.63)	-23.08 (1.58)	2.27 (1.56)	8.32 (5.27)
SE	D	>95%	1.35 (0.48)	-6.35 (2.68)	0.24 (0.16)	<b>-1.97</b> (0.91)	10.08 (0.84)	<b>6.94</b> (7.30)
		= Mean	-5.88 (0.25)	-6.52 (1.86)	3.02 (3.85)	-11.48 (0.28)	9.72 (0.75)	26.01 (18.35)
		<05%	-18.38 (2.80)	-5.10 (3.46)	7.16 (9.46)	<b>-21.54</b> (1.71)	9.06 (0.70)	<b>54.65</b> (27.06)
	C	>95%	0.79 (1.62)	-16.92 (2.03)	0.08 (0.03)	-7.31 (1.14)	2.11 (2.45)	3.82 (3.36)
		= Mean	-10.18 (0.31)	-15.66 (1.52)	1.14 (0.74)	-19.53 (0.28)	3.12 (1.13)	10.84 (7.42)
		<05%	-21.92 (1.41)	-13.81 (3.64)	3.15 (2.79)	-30.88 (1.67)	2.10 (1.00)	19.14 (7.26)
	E	>95%	-5.88 (1.03)	-13.48 (2.31)	0.30 (0.22)	-5.98 (1.52)	4.83 (2.06)	0.95 (1.80)
		= Mean	-14.92 (0.28)	-12.13 (2.35)	1.36 (1.44)	-16.42 (0.26)	6.21 (1.90)	2.73 (4.26)
		<05%	-23.9 (1.70)	-13.23 (3.23)	2.50 (3.07)	-26.96 (1.10)	6.19 (1.33)	8.45 (9.87)

<sup>a</sup>Bold numbers in Table 1 demonstrate the nonsystematic correlation between the changes in  $\delta^{18}\text{O}_p$  and changes in the precipitation amount

and vapor from the Indian Ocean (blue and green color) corresponds with mean and extreme low in  $\delta^{18}\text{O}_p$  (Figures 13e and 13f). The difference in the  $\delta^{18}\text{O}_p$  values within a group could be a result of the rainout from persistent precipitation. Vapor originating from west of the Arabian Sea in August corresponds with extreme high  $\delta^{18}\text{O}_p$  values (Figures 13b and 13e). The reasons could be that vapor sources from the ocean in the tropical region have a higher  $\delta^{18}\text{O}$  value than the continental sources in the midlatitude. Furthermore, a clear difference in the vapor source is found during January for location F (Figure 13a). The extreme low and mean  $\delta^{18}\text{O}_p$  values at location F originate from the west, and the vapor for extreme high  $\delta^{18}\text{O}_p$  values at location F originates from the Indian continent. Different from the above results, there are also rare cases in which a northwest vapor source coincides with extreme low  $\delta^{18}\text{O}_p$ , and the Indian Ocean vapor source coincides with extreme high  $\delta^{18}\text{O}_p$  (e.g., Figure 13d). In these cases, other factors other than the vapor source play a more important role.

#### 4.4. Comparisons of the Rayleigh Distillation Model (RDM) to the Tibetan Region GCM Simulations

The surface elevation history of the Himalaya-Tibet region is widely studied due to its importance as the largest orogenic plateau on Earth and allows for the study of climate and tectonic interactions. Applications of the RDM in paleoaltimetry studies [e.g., Rowley and Garzzone, 2007] have been preferred and widely used for interpreting modern and paleo  $\delta^{18}\text{O}_p$  observations because of the complexity and time-consuming nature of conducting GCM simulations. In this section, GCM-simulated  $\delta^{18}\text{O}_p$  and  $\delta^{18}\text{O}_p$  predicted by a RDM (forced with GCM output) was compared along one profile up the Himalaya front (averaged between 86 and 94°E) during the monsoon season (JAS). The initial conditions for the RDM are prescribed based on the GCM. The GCM-derived initial conditions for the RDM include the initial vapor temperature ( $T_v$ ) 28.4°C, initial vapor specific humidity ( $q_s$ ) 16.8 g/kg, and initial vapor  $\delta^{18}\text{O}_v$  of -13.0‰ (Figure 14a).

The two modeling approaches show an agreement whereby GCM  $\delta^{18}\text{O}_p$  differs from the RDM predictions near the surface and at ~2 km and >4 km elevation. The maximum difference between the two approaches in Figure 14a is <1‰, which is notably less than the difference of >3‰ observed in the North American Cordillera region [Feng et al., 2013]. Feng et al. [2013] evaluated the non-Rayleigh influences on the  $\delta^{18}\text{O}_p$  in and around the North American Cordillera and demonstrated the significant influence of atmosphere processes on  $\delta^{18}\text{O}_p$  including shifts in local precipitation types (e.g., from precipitation to snow or from large-scale precipitation to convective precipitation), development of air mixing, low-level vapor recycling (defined as the ratio of the evaporation to the precipitation), and changes in the vapor source. Among

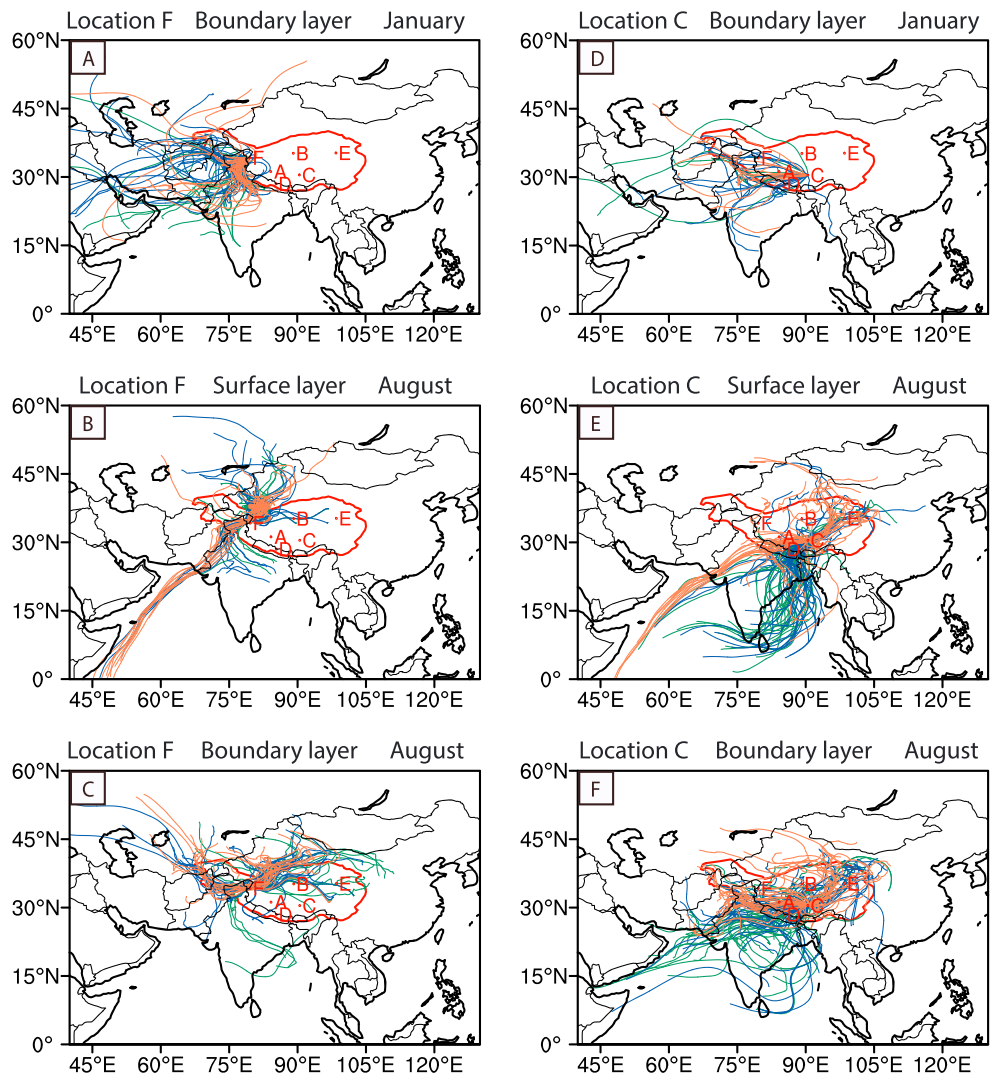


**Figure 13.** Backward trajectories for the extreme  $\delta^{18}O_p$  condition at (a–c) location F and (d–f) location C during January for the boundary layer (Figures 13a and 13d) and August for the surface layer (Figures 13b and 13e) and boundary layer (Figures 13c and 13f). Orange color shows the trajectories for the days with extreme high  $\delta^{18}O_p$  values, blue color shows that for the days with mean  $\delta^{18}O_p$  values, and green color represents that for the days with extreme low  $\delta^{18}O_p$  values.

these atmosphere processes, the low-level vapor recycling south of the Himalaya is about 10–30% which has no significant influence on the RDM calculation. The precipitation type is assumed to not change during the monsoon season. The difference between the Himalaya and North American Cordillera is likely due to the weaker upslope flow in Tibet and the higher specific humidity of monsoonal air parcels compared to air parcels over North America. As seen in Figure 14b, the airflow is blocked at the Himalaya front, forming a vertical cell. This amount of upslope flow cannot contribute to high-altitude mixing along the flanks [Galewsky, 2009]. Analyses of the upper limits of the mixing rate support this conclusion (Figure 14b). For example, the  $\delta^{18}O_p$  mixing rate exchange of an air parcel with the surrounding environment is  $<0.2\%$  across the Himalaya (Figure 14b), which suggests that the parcels undergo less mixing when convection is strong. The comparison between the RDM and GCM in this study suggests that the adiabatic process is the main control on  $\delta^{18}O_p$  at the Himalaya topographic front during the monsoon season. Our findings support the use of the RDM for modern conditions across the Himalaya front. However, this result may not be applicable to other regions neighboring Tibet and evaluation of the RDM approach for other locations and for paleoconditions when topography or wind trajectories may significantly differ requires additional verification.

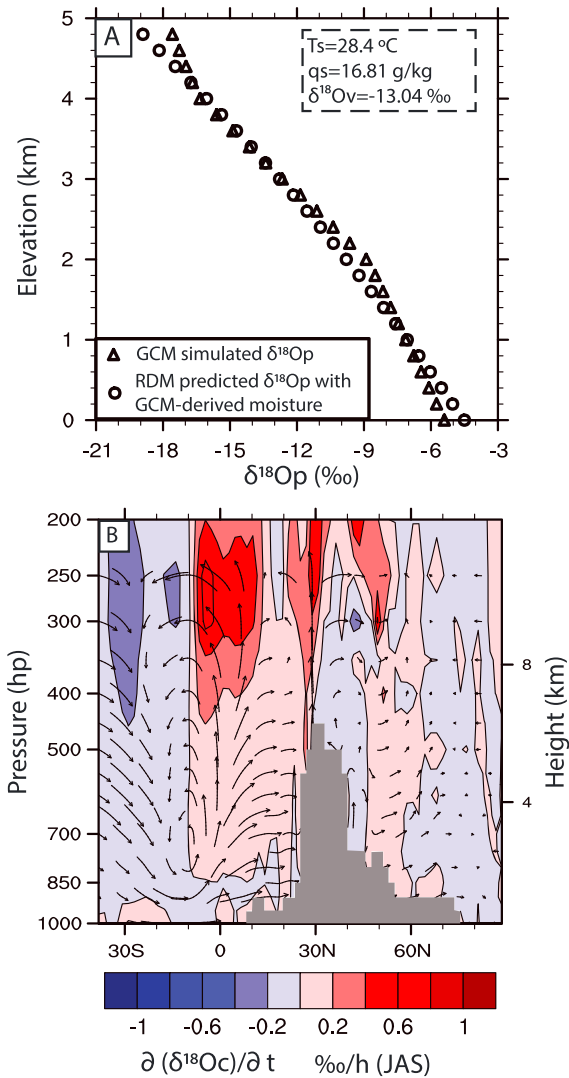


**Figure 14.** (a) Comparison of  $\delta^{18}O_p$  simulated by the GCM (triangle) and RDM (circle) approaches. GCM-derived moisture was used for the RDM start up. (b) Estimated  $\delta^{18}O_p$  mixing for monsoon season (JAS) perpendicular to the Himalaya (86°E–94°E). The Tibetan Plateau is shaded in gray. The vectors show zonally averaged meridional and vertical wind.

### 5. Conclusions

The main conclusions drawn from this study are the following.

1. Agreement exists between model-simulated  $\delta^{18}O_p$  and 2 years of observations on the Tibetan Plateau [Tian et al., 2007]. This conclusion confirms the overall good performance of the ECHAM5-wiso for the Tibetan Plateau region. The simulations also successfully predicted simulated seasonal trends in  $\delta^{18}O_p$  for different zones. Disagreements are noticeable in the model's overestimation of  $\delta^{18}O_p$  during the winter in the western Tibetan Plateau.
2. Large daily  $\delta^{18}O_p$  variations of  $-25$  to  $+5$ ‰ are documented for the 30 simulations years across the region as well as seasonal variation of 5 to 10‰ and interannual variation of 1.2 to 3.5‰. This result suggests that caution should be taken when interpreting short-term (from season to season or between years)  $\delta^{18}O_p$  observations as representative of climatic conditions ( $>= 30$  years).
3. Our results are at odds with previous studies that define north-to-south  $\delta^{18}O_p$  distribution zones [Tian et al., 2007; Yao et al., 2013] in that the zones are best divided along the direction of northeast to southwest. In the northwest zone, winter  $\delta^{18}O_p$  is low and summer  $\delta^{18}O_p$  is high. The seasonal variation in  $\delta^{18}O_p$  is about  $\pm 10$ ‰. The vapor originates from the arid western region of the Tibetan

Plateau, the low vapor content in the source region results in low precipitation on the Tibetan Plateau. In the southeast zone of the Tibetan Plateau, the seasonal  $\delta^{18}\text{O}_p$  signal is the opposite of that in the northeast zone.  $\delta^{18}\text{O}_p$  is low in the summer and high in the winter with a difference of  $\pm 15\text{‰}$ . This region is under the influence of the Indian and East Asian monsoon system and receives large amounts of precipitation in summer. In the transition zone (middle zone),  $\delta^{18}\text{O}_p$  is low in the winter and higher in the summer but the difference is smaller with about  $\pm 5\text{‰}$ .

4. Spatial and temporal variation of  $\delta^{18}\text{O}_p$  and isotopic lapse rates were analyzed.  $\delta^{18}\text{O}_p$  lapse rates of  $\sim -3.1\text{‰/km}$  are present in both the winter and summer season at the Himalayan front of the Tibetan Plateau. At the western side of the Tibetan Plateau a lapse rate of  $\sim -3.4\text{‰/km}$  was observed in the winter, and the lapse rate decreases to  $-1.7\text{‰/km}$  in the summer.
5. Zonal wind patterns and trajectories indicate a seasonal difference of  $\delta^{18}\text{O}_p$  vapor sources. Vapor originates from the western arid region in the winter and is delivered across most the Tibetan Plateau. The middle and southeast zones of the Tibetan Plateau receive summer vapor from the Indian Ocean. The vapor source influences  $\delta^{18}\text{O}_p$  because air masses with different vapor sources have different starting isotope fractions that have an influence on the isotope composition at a target region [e.g., *Bowen and Revenaugh, 2003*].
6. Our analysis for the causes of extreme  $\delta^{18}\text{O}_p$  shows that extreme high  $\delta^{18}\text{O}_p$  values correspond with lower precipitation rates for specific locations. Furthermore, there is no relationship between temperature and extreme low or high  $\delta^{18}\text{O}_p$  values. Vapor source has been shown to be an important control on the  $\delta^{18}\text{O}_p$  during the Indian monsoon season for the monsoon-influenced regions. Vapor from the north and southwest (especially from west of the Arabian Sea) generally coincides with extreme high  $\delta^{18}\text{O}_p$  daily values, while vapor from the Indian Ocean results in mean to extreme low  $\delta^{18}\text{O}_p$  values. Therefore, variations in vapor source are interpreted to be one important cause of the spatial-temporal differences in  $\delta^{18}\text{O}_p$ .
7. The agreement between the RDM- and ECHAM5-wiso-simulated  $\delta^{18}\text{O}_p$  at the Himalaya front ( $86^\circ\text{E}$ – $94^\circ\text{E}$ ) during the monsoon season suggests that the simplified RDM approach for estimating lapse rates is appropriate at this location under modern-day conditions. GCM  $\delta^{18}\text{O}_p$  differs from the RDM results at the near surface ( $\sim 2\text{ km}$ ) and at  $>4\text{ km}$  elevation with a maximum difference of  $<1\text{‰}$ . The changes in  $\delta^{18}\text{O}_p$  due to the exchange of an air parcel with the surrounding environment at the Himalaya front are not significant, and the mixing rate is less than  $0.2\text{‰/h}$ .

#### Acknowledgments

This work was supported by a German Science Foundation grant (DFG-EH329/2-1) to T. Ehlers through the German Science Foundation (DFG) Priority Program 1372 (Tibetan Plateau: Formation, Climate, Ecosystems). We thank the DKRZ computing center in Hamburg, Germany, for cluster computing time used for this study. The data are available from the authors upon request (todd.ehlers@uni-tuebingen.de). Two anonymous reviewers are thanked for their constructive reviews of the manuscript.

#### References

- Armengaud, A., R. Koster, J. Jouzel, and P. Ciais (1998), Deuterium excess in Greenland snow: Analysis with simple and complex models, *J. Geophys. Res.*, *103*, 8947–8953, doi:10.1029/98JD00274.
- Battisti, D. S., Q. Ding, and G. H. Roe (2014), Coherent pan-Asian climatic and isotopic response to orbital forcing of tropical insolation, *J. Geophys. Res. Atmos.*, *119*, 11,997–12,020, doi:10.1002/2014JD021960.
- Bertó, A. (2005), Lagrangian trajectory analysis for the identification of moist airflows producing intense precipitation events over the Alps, 223 pp., University of Trento.
- Boos, W. R., and Z. Kuang (2010), Dominant control of the South Asian monsoon by orographic insulation versus plateau heating, *Nature*, *463*, 218–222.
- Bowen, G. J., and J. Revenaugh (2003), Interpolating the isotopic composition of modern meteoric precipitation, *Water Resour. Res.*, *39*(10), 1299, doi:10.1029/2003WR002086.
- Butzin, M., M. Werner, V. Masson-Delmotte, C. Risi, C. Frankenberg, K. Gribanov, J. Jouzel, and V. I. Zakharov (2014), Variations of oxygen-18 in West Siberian precipitation during the last 50 years, *Atmos. Chem. Phys.*, *14*, 5853–5869, doi:10.5194/acp-14-5853-2014.
- Cole, J. E., R. D. Rind, R. S. Webb, J. Jouzel, and R. Healy (1999), Climatic controls on interannual variability of precipitation  $\delta^{18}\text{O}$ : The simulated influence of temperature, precipitation amount and vapor source region, *J. Geophys. Res.*, *104*, 14,223–14,235, doi:10.1029/1999JD900182.
- DeCelles, P. G., J. Quade, P. Kapp, M. J. Fan, D. L. Dettman, and L. Ding (2007), High and dry in central Tibet during the Late Oligocene, *Earth Planet. Sci. Lett.*, *253*(3–4), 389–401.
- Ehlers, T. A., and C. J. Poulsen (2009), Influence of Andean uplift on climate and paleoaltimetry estimates, *Earth Planet. Sci. Lett.*, *281*(3–4), 238–248.
- Feng, R., C. J. Poulsen, M. Werner, C. P. Chamberlain, H. T. Mix, and A. Mulch (2013), Early Cenozoic evolution of topography, climate, and stable isotopes in precipitation in the North American Cordillera, *Am. J. Sci.*, *313*, 613–648, doi:10.2475/07.3013.01.
- Gao, J., S. S. P. Shen, T. Yao, N. Tafolla, C. Risi, and Y. He (2015), Reconstruction of precipitation  $\delta^{18}\text{O}$  over the Tibetan Plateau since 1910, *J. Geophys. Res. Atmos.*, *120*, 4878–4888, doi:10.1002/2015JD023233.
- Galewsky, J. (2009), Orographic precipitation isotopic ratios in stratified atmospheric flows: Implications for paleoelevation studies, *Geology*, *37*(9), 791–794, doi:10.1130/G30008A.1.
- Garzione, C. N. (2008), Research focus surface uplift of Tibet and Cenozoic global cooling, *Geology*, *36*(12), 1003–1004.
- Graham, S. A., C. P. Chamberlain, Y. J. Yue, B. D. Ritts, A. D. Hanson, T. W. Horton, J. R. Waldbauer, M. A. Poage, and X. Feng (2005), Stable isotope records of Cenozoic climate and topography, Tibetan Plateau and Tarim Basin, *Am. J. Sci.*, *305*(2), 101–118.
- He, Y., et al. (2015), Impact of atmospheric convection on south Tibet summer precipitation isotopologue composition using a combination of in situ measurements, satellite data, and atmospheric general circulation modeling, *J. Geophys. Res. Atmos.*, *120*, 3852–3871, doi:10.1002/2014JD022180.

- Hoffmann, G., M. Werner, and M. Heimann (1998), Water isotope module of the ECHAM atmospheric general circulation model: A study on timescales from days to several years, *J. Geophys. Res.*, *103*, 23,323–23,323, doi:10.1029/98JD02857.
- Hren, M. T., B. Bookhagen, P. M. Blisniuk, A. L. Booth, and C. P. Chamberlain (2009), Delta O-18 and delta D of streamwaters across the Himalaya and Tibetan Plateau: Implications for moisture sources and paleoelevation reconstructions, *Earth and Planet. Sci. Lett.*, *288*(1–2), 20–32.
- Insel, N., C. J. Poulsen, T. A. Ehlers, and C. Sturm (2012), Response of meteoric  $\delta^{18}\text{O}$  to surface uplift—Implications for Cenozoic Andean Plateau growth, *Earth Planet. Sci. Lett.*, *317*, 262–272.
- Insel, N., C. J. Poulsen, C. Sturm, and T. A. Ehlers (2013), Climate controls on Andean precipitation  $\delta^{18}\text{O}$  interannual variability, *J. Geophys. Res. Atmos.*, *118*, 9721–9742, doi:10.1002/jgrd.50619.
- Jeffery, M. L., C. J. Poulsen, and T. A. Ehlers (2012), Impacts of global cooling, surface uplift and an inland seaway on South American paleoclimate and precipitation  $\delta^{18}\text{O}$ , *Geol. Soc. Am. Bull.*, *124*, 335–351.
- Jouzel, J., G. Hoffmann, R. D. Koster, and V. Masson (2000), Water isotopes in precipitation: Data/model comparison for present-day and past climates, *Quat. Sci. Rev.*, *19*, 363–379.
- Langebroek, P. M., M. Werner, and G. Lohmann (2011), Climate information imprinted in oxygen-isotopic composition of precipitation in Europe, *Earth Planet. Sci. Lett.*, *311*(1–2), 144–154.
- Liu, Z. F., L. D. Tian, T. D. Yao, and W. S. Yu (2010), Characterization of precipitation delta O-18 variation in Nagqu, central Tibetan Plateau and its climatic controls, *Theor. Appl. Climatol.*, *99*(1–2), 95–104.
- Ma, D., W. R. Boos, and Z. Kuang (2014), Effects of orography and surface heat fluxes on the South Asian summer monsoon, *J. Clim.*, *27*, 6647–6659.
- Majoube, M. (1971), Fractionnement en oxygen 18 et en deuterium entre l'eau et sa vapeur, *J. Chim. Phys.*, *68*(10), 1423–1436.
- Nakicenovic, N., J. Alcamo, G. Davis, B. de Vries, J. Fenhann, S. Gaffin, and K. Gregory (2000), *Special Report on Emissions Scenarios: A Special Report of Working Group III of the Intergovernmental Panel on Climate Change*, Cambridge Univ. Press, New York.
- Mutz, S. G., T. A. Ehlers, J. Li, C. Steger, H. Paeth, M. Werner, and C. J. Poulsen (2016), Precipitation  $\delta^{18}\text{O}$  over the Himalaya-Tibet Orogen from ECHAM5-wiso simulations: Statistical analysis of temperature, topography, and precipitation, *J. Geophys. Res. Atmos.*, doi:10.1002/2016JD024856.
- Poulsen, C. J., T. A. Ehlers, and N. Insel (2010), Onset of convective rainfall during gradual Late Miocene rise of the Central Andes, *Science*, *328*, 490–493.
- Roe, G. H., Q. Ding, D. S. Battisti, P. Molnar, M. L. Clark, and G. N. Garzzone (2016), A modeling study of the response of Asian summertime climate to the largest geologic forcings of the past 50 Ma, *J. Geophys. Res. Atmos.*, *121*, 5453–5470, doi:10.1002/2015JD024370.
- Roeckner, E., et al. (2003), The atmospheric general circulation model ECHAM5. Part I: Model description. Rep. 349Rep., 127 pp, Max Planck Institute for Meteorology, Hamburg.
- Rowley, D. B., and B. S. Currie (2006), Palaeo-altimetry of the late Eocene to Miocene Lunpola basin, central Tibet, *Nature*, *439*(7077), 677–681.
- Rowley, D. B., and C. N. Garzzone (2007), Stable isotope-based paleoaltimetry, *Annu. Rev. Earth Planet. Sci.*, *35*, 463–508.
- Ruddiman, W. F., and J. E. Kutzbach (1989), Forcing of late Cenozoic northern hemisphere climate by plateau uplift in southern Asia and the American west, *J. Geophys. Res.*, *94*, 18,409–18,427, doi:10.1029/JD094iD15p18409.
- Sherwood, S. C., R. Roca, T. M. Weckwerth, and N. G. Andronova (2010), Tropospheric water vapor, convection and climate, *Rev. Geophys.*, *48*, RG2001, doi:10.1029/2009RG000301.
- Sturm, C., F. Vimeux, and G. Krinner (2007), Intraseasonal variability in South America recorded in stable water isotopes, *J. Geophys. Res.*, *112*, D20118, doi:10.1029/2006JD008298.
- Tian, L., T. Yao, Z. Yang, and J. Pu (1997), A 4-year's observation of delta O-18 in precipitation on the Tibetan Plateau, *J. Glaciol. Geocryology*, *19*, 32–36.
- Tian, L. D., T. D. Yao, K. MacClune, J. W. C. White, A. Schilla, B. Vaughn, R. Vachon, and K. Ichiyangi (2007), Stable isotopic variations in west China: A consideration of moisture sources, *J. Geophys. Res.*, *112*, D10112, doi:10.1029/2006JD007718.
- Vuille, M., and M. Werner (2005), Stable isotopes in precipitation recording South American summer monsoon and ENSO variability: Observations and model results, *Clim. Dyn.*, *25*(4), 401–413.
- Vuille, M., M. Werner, R. S. Bradley, and F. Keimig (2005), Stable isotopes in precipitation in the Asian monsoon region, *J. Geophys. Res.*, *110*, 23108, doi:10.1029/2005JD006022.
- Werner, M., M. Heimann, and G. Hoffmann (1998), Stable water isotopes in Greenland ice cores: ECHAM 4 model simulations versus field measurements. In: IAEA, (Ed.) International Symposium on Isotopes Techniques in the study of Past and Current Environmental changes in the Hydrosphere and the Atmosphere. Vienna. 603–612.
- Werner, M., P. M. Langebroek, T. Carlsen, M. Herold, and G. Lohmann (2011), Stable water isotopes in the ECHAM5 general circulation model: Toward high-resolution isotope modeling on a global scale, *J. Geophys. Res.*, *116*, D15109, doi:10.1029/2011JD015681.
- Yao, T. D., V. Masson, J. Jouzel, M. Stievenard, W. Z. Sun, and K. Q. Jiao (1999), Relationships between delta O-18 in precipitation and surface air temperature in the Urumqi River Basin, east Tianshan Mountains, China, *Geophys. Res. Lett.*, *26*, 3473–3476, doi:10.1029/1999GL006061.
- Yao, T., et al. (2013), A review of climatic controls on in delta O-18 precipitation over the Tibetan Plateau: Observations and simulations, *Rev. Geophys.*, *51*, 525–548, doi:10.1002/rog.20023.
- Yurtsever, Y., and J. Gat (1981), Stable isotope hydrology: Deuterium and Oxygen-18 in the water cycle, *Atmospheric waters*, eds. Gat, J. R. and Gonfianini, R., IAEA, Vienna.